



RESEARCH ARTICLE

[View Article Online](#)
[View Journal](#) | [View Issue](#)Cite this: *RSC Med. Chem.*, 2023, 14, 2640**Novel pyrazolo[3,4-*d*]pyrimidine derivatives: design, synthesis, anticancer evaluation, VEGFR-2 inhibition, and antiangiogenic activity†**Ahmed M. Abdelhamed,^a Rasha A. Hassan,^b *^b
Hanan H. Kadry^b and Amira A. Helwa *^a

A novel series of 12 pyrazolo[3,4-*d*]pyrimidine derivatives were created and evaluated *in vitro* for their antiproliferative activity against the NCI 60 human tumor cell line panel. Compounds **12a–d** displayed significant antitumor activity against MDA-MB-468 and T-47D (breast cancer cell lines), especially compound **12b**, which exhibited the highest anticancer activity against MDA-MB-468 and T-47D cell lines with IC₅₀ values of 3.343 ± 0.13 and 4.792 ± 0.21 μM, respectively compared to staurosporine with IC₅₀ values of 6.358 ± 0.24 and 4.849 ± 0.22 μM. The most potent cytotoxic derivatives **12a–d** were studied for their VEGFR-2 inhibitory activity to explore the mechanism of action of these substances. Compound **12b** had potent activity against VEGFR-2 with an IC₅₀ value of 0.063 ± 0.003 μM, compared to sunitinib with IC₅₀ = 0.035 ± 0.012 μM. Moreover, there was an excellent reduction in HUVEC migratory potential that resulted in a significant disruption of wound healing patterns by 23% after 72 h of treatment with compound **12b**. Cell cycle and apoptosis investigations showed that compound **12b** could stop the cell cycle at the S phase and significantly increase total apoptosis in the MDA-MB-468 cell line by 18.98-fold compared to the control. Moreover, compound **12b** increased the caspase-3 level in the MDA-MB-468 cell line by 7.32-fold as compared to the control.

Received 8th September 2023,
Accepted 23rd October 2023

DOI: 10.1039/d3md00476g

rsc.li/medchem**Introduction**

Cancer, a global health concern, accounts for millions of deaths annually.¹ In 2020, the number of reported cancer cases reached 19.3 million, with nearly 10 million cancer-related deaths recorded.^{2,3} The development of novel therapies for cancer poses a significant challenge because of its complex and heterogeneous nature. Cancer often exhibits common traits, such as self-proliferation induction, resistance to apoptosis, unlimited proliferative potential, and high invasiveness, which can arise from the hyperactivation of oncogenic pathways and/or disruption of tumor suppressor mechanisms.^{4–7}

Protein tyrosine kinases (PTKs) are crucial enzymes that mediate their function by transferring the phosphoryl group from the gamma position of ATP, resulting in the phosphorylation of tyrosine residues in proteins.⁸ These

enzymes can be categorized based on their location as membrane-bound receptor tyrosine kinases (RTKs) or cytoplasmic non-receptor tyrosine kinases (NRTKs).⁸ PTKs play pivotal roles in regulating various essential cellular processes, including cell proliferation, growth, metabolism, motility, and apoptosis. Dysregulated PTK catalytic activity, often caused by mutations or overexpression, contributes significantly to several clinical diseases, including cancer.^{9–11} Substantial efforts have been dedicated to elucidating the physiological and pathological functions of receptor protein kinase signal transduction pathways over the past 35 years.⁸

The receptor tyrosine kinase superfamily includes three subtypes of vascular endothelial growth factor (VEGF) receptors, namely VEGFR-1–3. The extracellular domain of VEGFRs consists of approximately 750 amino acid residues and is organized into seven immunoglobulin (Ig)-like folds. VEGFR-1 and VEGFR-2 play critical roles in physiological and pathological angiogenesis, including tumor angiogenesis.¹¹

The VEGFR signaling pathway holds substantial importance as a therapeutic target for various human malignancies because it exerts significant control over tumor angiogenesis. VEGFR-2 is a crucial target for angiogenesis. Inhibition of the VEGF/VEGFR signaling pathway has shown promising potential for impeding tumor angiogenesis and tumor growth.¹² VEGFR-2 resembles a typical tyrosine kinase

^a Pharmaceutical Organic Chemistry Department, College of Pharmaceutical Sciences and Drug Manufacturing, Misr University for Science and Technology (MUST), 6th of October City, Egypt. E-mail: amira.helwa@must.edu.eg^b Pharmaceutical Organic Chemistry Department, Faculty of Pharmacy, Cairo University, Kasr El-Aini Street, Cairo 11562, Egypt.E-mail: rasha.hasan@pharma.cu.edu.eg† Electronic supplementary information (ESI) available. See DOI: <https://doi.org/10.1039/d3md00476g>

receptor and comprises an extracellular ligand-binding domain, a transmembrane domain, and a tyrosine kinase domain.¹³

VEGFR-2 inhibitors can be classified into three groups based on their binding positions to the receptor. Sunitinib (Fig. 1) belongs to the category of type I inhibitors, which competitively bind to the ATP-binding pocket in the active “DFG-in” conformation. It uses hydrogen bonds in the hinge region and hydrophobic interactions in the adenine region to establish binding interactions.¹⁴ Sorafenib (Fig. 1) is a type II inhibitor that occupies the inactive “DFG-out” conformation of the ATP-binding site and accesses the hydrophobic back pocket.^{14–17} Additionally, type III inhibitors bind to an inactive “DFG-out” conformation outside the ATP pocket. Recently, numerous VEGFR-2 inhibitors have been developed and used in cancer treatment. Notably, sunitinib and sorafenib have been approved for various types of cancer.^{18–20} Sunitinib, an indolinone-category kinase inhibitor, was first introduced on the market. It is prescribed to treat imatinib-resistant gastrointestinal stromal tumors and renal cell carcinoma.²¹ Sunitinib inhibits VEGFR-2 by binding to its kinase domain.²² Sunitinib and various VEGFR-2 inhibitors have been studied regarding their structure–activity relationship (SAR) and binding patterns. Studies have revealed four key characteristics of these inhibitors.^{23–25} First, most inhibitors exhibit an aromatic flat ring structure, occupying the ATP-binding domain and engaging in hydrogen bond interactions (shown in blue) with the Cys919 residues in the hinge region. In particular, sunitinib forms additional hydrogen bonds with Glu917.²¹ Second, an aryl ring acts as a hydrophobic spacer, occupying the region between the ATP-binding and DFG domains (shown in green). Third, VEGFR-2 inhibitors possess a linker that accepts and donates hydrogen bonds (HBA–HBD), establishing interactions (shown in red) with the DFG moiety residues (Glu885 and Asp1046). Finally, these inhibitors possess a terminal hydrophobic group that interacts with the

allosteric hydrophobic pocket through multiple hydrophobic interactions (shown in brown).

Developing novel anticancer medications, including kinase inhibitors, with improved tumor selectivity, efficacy, and safety remains a crucial objective in research. Among the isosteres of the purine nuclei, the pyrazolo[3,4-*d*]pyrimidine scaffold is widely recognized as one of the most desirable heterocycles for drug discovery, particularly in cancer therapy. Extensive investigations have revealed diverse pharmacological properties associated with this scaffold,^{26,27} with notable attributes of potent anticancer activity.^{28–30} Previous reports suggest that this scaffold exerts its anticancer effects through various distinct mechanisms, such as inhibition of cyclin-dependent kinases (CDK)^{31–33} and the epidermal growth factor receptor (EGFR).³⁴

The synthesized pyrazolo[3,4-*d*]pyrimidine compounds demonstrated significant potential as anticancer agents and have been identified as promising lead compounds for future cancer chemotherapy drugs. Fig. 2 illustrates a selection of both marketed VEGFR-2 inhibitors (sunitinib and sorafenib) and previously published pyrazolo[3,4-*d*]pyrimidine derivatives (I–VI), which have exhibited promising anticancer activity and VEGFR-2 inhibitory effects.^{29,35–39}

Building upon these findings and building on our previous research on anticancer derivatives,^{40–47} specifically focusing on VEGFR-2 inhibitors,^{48–53} the main objective of this study was to synthesize novel derivatives of pyrazolo[3,4-*d*]pyrimidine with anticancer activity, while possessing the fundamental pharmacophoric properties found in first-generation VEGFR-2 inhibitors such as sunitinib, through ring variation and bio isosteric replacement (Fig. 3). Subsequently, the anticancer activities of all the synthesized derivatives were evaluated using the NCI (USA) 60-panel cell line. The most potent derivatives were further assessed using the MTT assay against two breast cancer cell lines, MDA-MB-468 and T47D, and a normal breast cell line, MCF-10a. Furthermore, this study evaluated the *in vitro* VEGFR-2 inhibition of the most promising derivatives. Additionally, a wound healing test was conducted to assess the antiangiogenic properties of the most potent derivatives. Furthermore, the impact on the normal cell cycle profile, caspase-3 activity, and induction of apoptosis in the breast cancer cell line MDA-MB-468 was investigated. Finally, a molecular docking study was performed to validate the binding mode of the most active derivatives within the VEGFR-2 binding site.

In the designed compounds, the indolinone scaffold of sunitinib was substituted for a pyrazolo[3,4-*d*]pyrimidine core. Furthermore, the terminal *N,N,N*-triethylamine group of sunitinib was replaced with aliphatic, aromatic, and heterocyclic moieties. Additionally, some compounds, such as compounds 7, 11, and 12a–e, retained the amide spacer present in sunitinib, whereas others had the amide spacer removed, as seen in compounds 4, 8, and 9. Alternative spacers, including an azomethine group in derivative 10 and

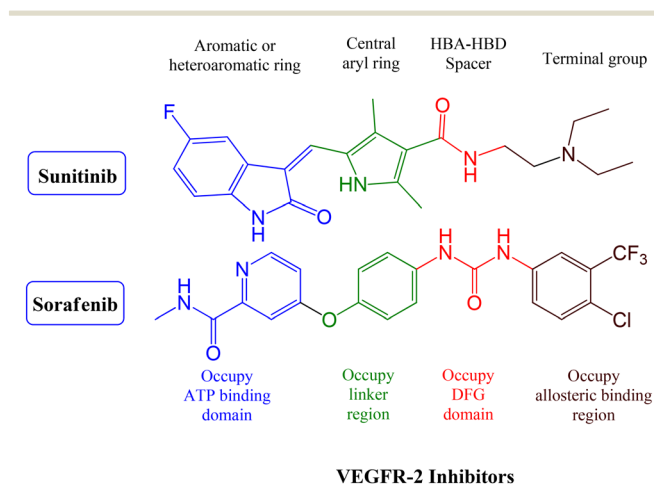


Fig. 1 Inhibitors of VEGFR-2 and their pharmacophoric properties.

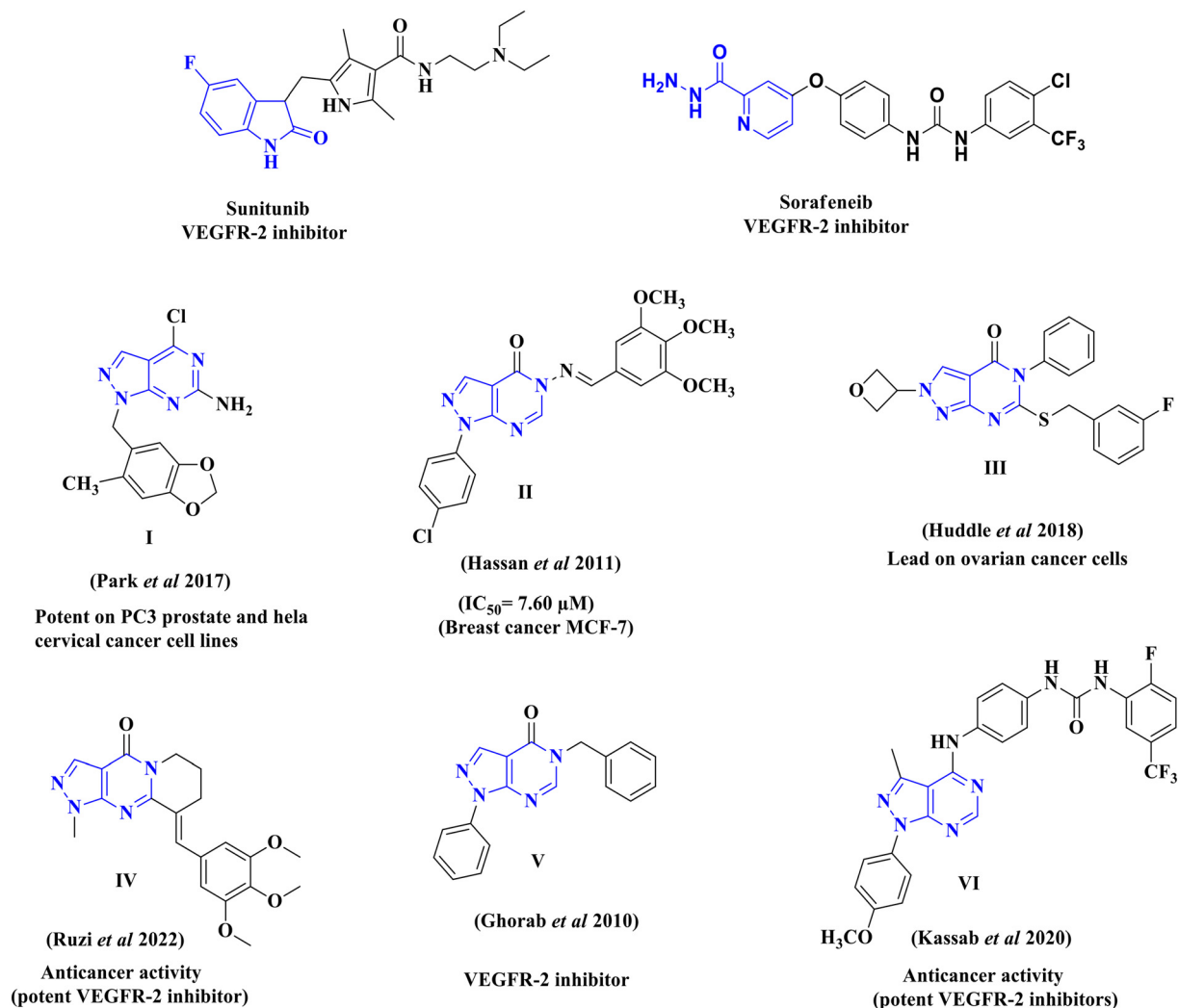


Fig. 2 Structures of reported pyrazolo[3,4-*d*]pyrimidine derivatives, and some VEGFR-2 inhibitors with cytotoxic activity.

an α , β -unsaturated carbonyl chain in derivative **6**, were introduced (Fig. 3).

Experimental section

Chemistry

General information. Melting points were obtained on a Griffin apparatus and were uncorrected. Microanalyses for C, H, and N were carried out at the Regional Center for Mycology and Biotechnology, Faculty of Pharmacy, Al-Azhar University. IR spectra were recorded on a Shimadzu IR 435 spectrophotometer (Shimadzu Corp., Kyoto, Japan), Faculty of Pharmacy, Cairo University, Cairo, Egypt. ¹H NMR spectra were measured on a Bruker 400 MHz (Bruker Corp., Billerica, MA, USA) spectrophotometer, Faculty of Pharmacy, Cairo University, Cairo, Egypt. ¹³C NMR spectra were obtained on a Bruker 100 MHz spectrophotometer, Faculty of Pharmacy. Electron ionization mass spectra (EI-MS) were obtained with a Thermo Scientific, ISQ Single Quadruple MS (Italy, USA) using 70 eV ionization energy at National Research Centre,

Cairo, Egypt. Compounds **1–3**, and **5** were prepared according to the reported procedures.^{54–56}

Procedure for preparation of 5-(4-aminophenyl)-6-methyl-1-phenyl-1*H*-pyrazolo[3,4-*d*]pyrimidin-4(5*H*)-one (4**).** To a mixture of compound **3** (2.27 g, 0.01 mol) in butanol (10 mL), *p*-phenylene diamine was added (1.08 g, 0.01 mol). The mixture was heated under reflux for 8 h. The precipitate formed while hot, filtered, dried, and crystallized from methanol to give a black solid: 45% yield; m.p. 250–252 °C; IR (KBr, cm⁻¹) 3447, 3420 (NH₂), 3011 (CH aromatic), 2934, 2895 (CH aliphatic), 1697 (C=O), 1600 (C=N), 1560 (C=C). ¹H NMR (400 MHz, DMSO-*d*₆) δ : 8.31 (s, 1H, CH pyrazole), 8.09 (d, *J* = 7.6 Hz, 2H, ArH), 7.58 (t, *J* = 7.6 Hz, 2H, ArH), 7.41 (t, *J* = 7.6 Hz, 1H, ArH), 6.97 (d, *J* = 8.4 Hz, 2H, ArH), 6.68 (d, *J* = 8.4 Hz, 2H, ArH), 5.44 (s, 2H, NH₂, D₂O exchangeable), 2.20 (s, 3H, CH₃); ¹³C NMR (100 MHz, DMSO-*d*₆) δ : 160.6, 158.3, 151.1, 149.7, 138.8, 136.7, 129.7 (2C), 129.0 (2C), 127.4, 125.6, 122.0 (2C), 114.6 (2C), 106.0, 25.2; EI-MS: *m/z* = 317 [M⁺] (100%); Anal. Calcd. for C₁₈H₁₅N₅O: C, 68.13; H, 4.76; N, 22.07; found C, 67.91; H, 4.89; N, 21.98.

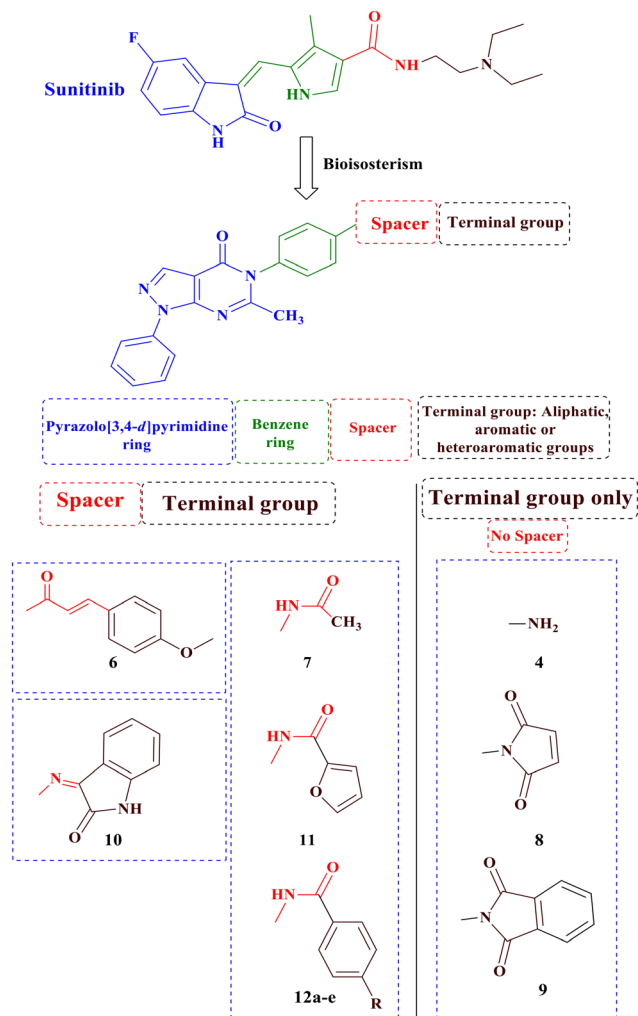


Fig. 3 Rationale design of the novel pyrazolo[3,4-d]pyrimidine as VEGFR-2 inhibitors comparative to sunitinib's pharmacophoric properties.

Procedure for preparation of (*E*)-5-(4-(3-(4-methoxyphenyl)acryloyl)phenyl)-6-methyl-1-phenyl-1*H*-pyrazolo[3,4-*d*]pyrimidin-4(5*H*)-one (6). *p*-Methoxybenzaldehyde (1.36 g, 0.01 mol) was added to a solution of compound 5 (3.57 g, 0.01 mol) in 10 mL of absolute ethanol and 2.0 mL of 40% NaOH. The resulting mixture was then stirred at room temperature for 3 h. The precipitate formed was filtered, dried, and crystallized in ethyl alcohol, resulting in a yellow solid: 56% yield; m.p. 225–227 °C; IR (KBr, cm⁻¹) 3047, 3001 (CH aromatic), 2978, 2889 (CH aliphatic), 1693, 1685 (2 C=O), 1593 (C=N), 1508 (C=C), ¹H NMR (400 MHz, DMSO-*d*₆) δ; 8.32 (s, 1H, CH pyrazole), 8.19 (d, *J* = 8.8 Hz, 2H, ArH), 7.93 (d, *J* = 8.8 Hz, 2H, ArH), 7.88–7.82 (m, 2H, ArH), 7.72 (d, *J* = 15.6 Hz, 2H, CH=CH), 7.59–7.51 (m, 4H, ArH), 7.46–7.42 (m, 1H, ArH), 7.03 (d, *J* = 8.8 Hz, 2H, ArH), 3.83 (s, 3H, OCH₃), 1.97 (s, 3H, CH₃); ¹³C NMR (100 MHz, DMSO-*d*₆) δ; 187.9, 170.6, 161.7, 161.0, 144.0, 143.8, 140.1, 138.8, 133.0, 132.3, 131.2 (2C), 130.1 (2C), 129.6 (2C), 128.4, 127.9 (2C), 124.0 (2C), 120.0, 119.5, 115.0 (2C), 114.9, 55.8, 23.4; EI-MS: *m/z* =

462 [M⁺] (1.51%); Anal. Calcd. for C₂₈H₂₂N₄O₃: C, 72.71; H, 4.79; N, 12.11; found C, 72.86; H, 4.96; N, 12.32.

***N*-(4-(6-Methyl-4-oxo-1-phenyl-1*H*-pyrazolo[3,4-*d*]pyrimidin-5(4*H*)-yl)phenyl)acetamide (7).** A mixture of compound 4 (3.17 g, 0.01 mol) in glacial acetic acid (10 mL) was heated under reflux for 16 h and the resulting solid was filtered and dried to give a light green solid: 45% yield; m.p. 245–247 °C; IR (KBr, cm⁻¹) 3414 (NH), 3124, 3066 (CH aromatic), 2931, 2870 (CH aliphatic), 1697 broad peak (2 C=O), 1600 (C=N), 1543 (C=C). ¹H NMR (400 MHz, DMSO-*d*₆) δ; 10.18 (s, 1H, NH, D₂O exchangeable), 8.35 (s, 1H, CH pyrazole), 8.10 (d, *J* = 8.0 Hz, 2H, ArH), 7.75 (d, *J* = 8.8 Hz, 2H, ArH), 7.59 (t, *J* = 8.0 Hz, 2H, ArH), 7.42 (t, *J* = 7.4 Hz, 1H, ArH), 7.34 (d, *J* = 8.8 Hz, 2H, ArH), 2.19 (s, 3H, CH₃), 2.10 (s, 3H, CH₃); ¹³C NMR (100 MHz, DMSO-*d*₆) δ; 169.3, 159.8, 158.1, 151.1, 140.2, 138.7, 136.7, 132.5, 129.7 (2C), 129.2 (2C), 127.6, 122.2 (2C), 120.2 (2C), 105.9, 25.1, 24.4; EI-MS: *m/z* = 359 [M⁺] (46.62%); Anal. Calcd. for C₂₀H₁₇N₅O₂: C, 66.84; H, 4.77; N, 19.49; found C, 67.12; H, 4.89; N, 19.72.

1-(4-(6-Methyl-4-oxo-1-phenyl-1*H*-pyrazolo[3,4-*d*]pyrimidin-5(4*H*)-yl)phenyl)-1*H*-pyrrole-2,5-dione (8). Compound 4 (3.17 g, 0.01 mol) was combined with glacial acetic acid (10 mL). Maleic anhydride (1.08 g, 0.011 mol) was added to the solution, which was then heated under reflux for 16 h. The resulting precipitate was filtered while hot and subsequently crystallized from absolute ethanol, resulting in a gray solid: 47% yield; m.p. 315–317 °C; IR (KBr, cm⁻¹) 3163, 3067 (CH aromatic), 2974, 2939 (CH aliphatic), 1712–1697 (3 C=O), 1566 (C=N), 1508 (C=C). ¹H NMR (400 MHz, DMSO-*d*₆) δ; 8.39 (s, 1H, CH pyrazole), 8.11 (d, *J* = 7.4 Hz, 2H, ArH), 7.62–7.55 (m, 6H, ArH), 7.43 (t, *J* = 7.4 Hz, 1H, ArH), 7.26 (s, 2H, ArH), 2.22 (s, 3H, CH₃); ¹³C NMR (100 MHz, DMSO-*d*₆) δ; 170.2 (2C), 159.4, 158.0, 151.2, 138.7, 137.0, 136.8, 135.3 (2C), 132.6, 129.8 (2C), 129.6 (2C), 128.1, 127.6 (2C), 122.1 (2C), 105.9, 25.3; EI-MS: *m/z* = 397 [M⁺] (100%); Anal. Calcd. for C₂₂H₁₅N₅O₃: C, 66.49; H, 3.80; N, 17.62; found C, 66.72; H, 4.01; N, 17.85.

2-(4-(6-Methyl-4-oxo-1-phenyl-1*H*-pyrazolo[3,4-*d*]pyrimidin-5(4*H*)-yl)phenyl)isoindoline-1,3-dione (9). In a reaction mixture containing compound 4 (3.17 g, 0.01 mol) and glacial acetic acid (10 mL), phthalic anhydride (1.62 g, 0.011 mol) was introduced. The solution was refluxed for 16 h, and its precipitate was filtered while still hot. Subsequently, the precipitate was crystallized from absolute ethanol, resulting in a gray solid: 58% yield; m.p. 320–322 °C; IR (KBr, cm⁻¹) 3062, 3008 (CH aromatic), 2931, 2777 (CH aliphatic), 1716, 1681, 1643 (3 C=O), 1600 (C=N), 1508 (C=C). ¹H NMR (400 MHz, DMSO-*d*₆) δ; 8.36 (s, 1H, CH pyrazole), 8.12–8.10 (m, 2H, ArH), 8.03–7.94 (m, 2H, ArH), 7.92–7.87 (m, 2H, ArH), 7.71–7.68 (m, 1H, ArH), 7.64–7.58 (m, 4H, ArH), 7.45–7.42 (m, 1H, ArH), 7.39 (d, *J* = 8.8 Hz, 1H, ArH), 2.24 (s, 3H, CH₃); ¹³C NMR (100 MHz, DMSO-*d*₆) δ; 168.1, 167.8, 167.3, 159.8, 158.1, 151.1, 138.8, 136.8, 132.0, 129.8 (4C), 129.2, 128.8, 127.6, 124.0 (2C), 122.1 (4C), 120.7 (2C), 105.9, 25.3. EI-MS: *m/z* = 447 [M⁺] (5.46%); Anal. Calcd. for C₂₆H₁₇N₅O₃: C, 69.79; H, 3.83; N, 15.65; found C, 69.57; H, 3.98; N, 15.87.

6-Methyl-5-(4-((2-oxoindolin-3-ylidene)amino)phenyl)-1-phenyl-1H-pyrazolo[3,4-*d*]pyrimidin-4(5*H*)-one (10). A mixture of compound **4** (3.17 g, 0.01 mol) and glacial acetic acid (10 mL) was combined with isatin (1.62 g, 0.011 mol). The solution was heated under reflux for 16 h, followed by the filtration of the hot precipitate. The precipitate was crystallized from absolute ethanol, resulting in a dark green solid: 41% yield; m.p. 300–302 °C; IR (KBr, cm⁻¹) 3252 (NH Str), 3059, 3001 (CH aromatic), 2877, 2785 (CH aliphatic), 1732, 1693, 1659 (3 C=O), 1600 (C=N), 1500 (C=C). ¹H NMR (400 MHz, DMSO-*d*₆) δ: 11.14 (s, 1H, NH, D₂O exchangeable), 8.39 (s, 1H, CH pyrazole), 8.12 (d, *J* = 8.0 Hz, 2H, ArH), 7.61 (t, *J* = 8.0 Hz, 2H, ArH), 7.54 (d, *J* = 8.4 Hz, 1H, ArH), 7.46–7.36 (m, 3H, ArH), 7.19 (d, *J* = 8.4 Hz, 2H, ArH), 6.96 (d, *J* = 7.6 Hz, 1H, ArH), 6.75 (t, *J* = 7.6 Hz, 1H, ArH), 6.44 (d, *J* = 7.6 Hz, 1H, ArH), 2.23 (s, 3H, CH₃); ¹³C NMR (100 MHz, DMSO-*d*₆) δ: 163.8, 159.7, 158.1, 156.1, 151.6, 151.2, 147.7, 138.7, 136.8, 135.2, 134.6, 130.4 (2C), 129.8 (2C), 127.6, 126.0, 122.2 (2C), 118.9 (2C), 116.2, 112.2, 106.0, 96.8, 25.2; EI-MS: *m/z* = 446 [M⁺] (11.97%); Anal. Calcd. for C₂₆H₁₈N₆O₂: C, 69.95; H, 4.06; N, 18.82; found C, 70.18; H, 4.24; N, 19.08.

***N*-(4-(6-Methyl-4-oxo-1-phenyl-1H-pyrazolo[3,4-*d*]pyrimidin-5(4*H*)-yl)phenyl)furan-2-carboxamide (11).** Compound **4** (3.17 g, 0.01 mol) and furoyl chloride (1.30 g, 0.01 mol) were dissolved in dry benzene (10 mL) in the presence of anhydrous potassium carbonate (1.38 g, 0.01 mol). The reaction mixture was refluxed for 24 h. The resulting precipitate was filtered, dried, and crystallized from the ethanol to yield a gray solid: 43% yield; m.p. 300–302 °C IR (KBr, cm⁻¹) 3464 (NH), 3109, 3043 (CH aromatic), 2908, 2839 (CH aliphatic), 1685 broad peak (2 C=O), 1566 (C=N), 1508 (C=C). ¹H NMR (400 MHz, DMSO-*d*₆) δ: 10.57 (s, 1H, NH, D₂O exchangeable), 8.36 (s, 1H, CH pyrazole), 8.11 (d, *J* = 7.6 Hz, 2H, ArH), 8.03 (d, 2H, ArH), 7.97 (d, *J* = 8.8 Hz, 2H, ArH), 7.65 (d, *J* = 8.8 Hz, 2H, ArH), 7.59 (t, *J* = 8.8 Hz, 2H, ArH), 7.42 (d, *J* = 8.8 Hz, 2H, ArH), 2.23 (s, 3H, CH₃); ¹³C NMR (100 MHz, DMSO-*d*₆) δ: 165.2, 159.7, 158.1, 151.1, 140.0, 138.7, 137.1, 136.8, 133.9, 133.2, 130.2, 130.0, 129.8, 129.2, 129.0, 128.9, 128.8, 127.6, 122.1, 121.6, 121.2, 105.9, 25.2; EI-MS: *m/z* = 412 [M⁺ + H] (0.73%); Anal. Calcd. for C₂₃H₁₇N₅O₂: C, 67.15; H, 4.17; N, 17.02; found C, 67.43; H, 4.25; N, 17.31.

General procedure for the preparation of *N*-(4-(6-methyl-4-oxo-1-phenyl-1H-pyrazolo[3,4-*d*]pyrimidin-5(4*H*)-yl)aryl)benzamid derivatives (12a–e). Compound **4** (3.17 g, 0.01 mol) was mixed with the corresponding benzoyl chloride (0.01 mol) in dry benzene (10 mL) containing anhydrous potassium carbonate (1.38 g, 0.01 mol). The reaction mixture was refluxed for 24 h. The resulting solid was filtered, heated, dried, and crystallized in ethanol.

***N*-(4-(6-Methyl-4-oxo-1-phenyl-1H-pyrazolo[3,4-*d*]pyrimidin-5(4*H*)-yl)phenyl)benzamide (12a).** Gray solid: 90% yield; m.p. 308–310 °C; IR (KBr, cm⁻¹) 3356 (NH), 3062, 3005 (CH aromatic), 2970, 2916 (CH aliphatic), 1705, 1659 (2 C=O), 1550 (C=N), 1508 (C=C). ¹H NMR (400 MHz, DMSO-*d*₆) δ: 10.50 (s, 1H, NH, D₂O exchangeable), 8.37 (s, 1H, CH pyrazole), 8.11 (d, *J* = 8.0 Hz, 2H, ArH), 7.99 (t, *J* = 7.6 Hz, 4H,

ArH), 7.65–7.55 (m, 5H, ArH), 7.45–7.41 (m, 3H, ArH), 2.23 (s, 3H, CH₃); ¹³C NMR (100 MHz, DMSO-*d*₆) δ: 166.4, 159.8, 158.1, 151.2, 140.2, 138.7, 136.8, 135.2, 133.1, 132.2, 129.8 (2C), 129.2 (2C), 128.9 (2C), 128.2 (2C), 127.6, 122.2 (2C), 121.5 (2C), 105.9, 25.2; EI-MS: *m/z* = 421 [M⁺] (1.55%); Anal. Calcd. for C₂₅H₁₉N₅O₂: C, 71.25; H, 4.54; N, 16.62; found C, 70.98; H, 4.63; N, 16.89.

4-Fluoro-*N*-(4-(6-methyl-4-oxo-1-phenyl-1H-pyrazolo[3,4-*d*]pyrimidin-5(4*H*)-yl)phenyl)benzamide (12b). Gray solid: 50% yield; m.p. 310–312 °C; IR (KBr, cm⁻¹) 3298 (NH), 3051, 3001 (CH aromatic), 2932, 2900 (CH aliphatic), 1694, 1670 (2 C=O), 1566 (C=N), 1504 (C=C). ¹H NMR (400 MHz, DMSO-*d*₆) δ: 10.50 (s, 1H, NH, D₂O exchangeable), 8.36 (s, 1H, CH pyrazole), 8.12–8.06 (m, 4H, ArH), 7.96 (d, *J* = 8.4 Hz, 2H, ArH), 7.60 (t, *J* = 8.0 Hz, 2H, ArH), 7.45–7.37 (m, 5H, ArH), 2.23 (s, 3H, CH₃); ¹³C NMR (100 MHz, DMSO-*d*₆) δ: 165.3, 163.4, 159.7, 158.2, 151.1, 140.0, 138.6, 136.7, 133.1, 131.6, 131.0, 130.9, 129.7 (2C), 129.1(2C), 127.6, 122.2 (2C), 121.7 (2C), 116.0, 115.8, 105.8, 25.1; EI-MS: *m/z* = 439 [M⁺] (73.26%); Anal. Calcd. for C₂₅H₁₈FN₅O₂: C, 68.33; H, 4.13; N, 15.94; found C, 68.56; H, 4.29; N, 16.12.

4-Chloro-*N*-(4-(6-methyl-4-oxo-1-phenyl-1H-pyrazolo[3,4-*d*]pyrimidin-5(4*H*)-yl)phenyl)benzamide (12c). Gray solid: 46% yield; m.p. 303–305 °C; IR (KBr, cm⁻¹) 3294 (NH), 3043, 3012 (CH aromatic), 2978, 2924 (CH aliphatic), 1690, 1651 (2 C=O), 1550 (C=N), 1508 (C=C). ¹H NMR (400 MHz, DMSO-*d*₆) δ: 10.58 (s, 1H, NH, D₂O exchangeable), 8.36 (s, 1H, CH pyrazole), 8.10 (d, *J* = 7.6 Hz, 2H, ArH), 7.98 (d, *J* = 8.8 Hz, 4H, ArH), 7.60 (t, *J* = 8.0 Hz, 2H, ArH), 7.51 (d, *J* = 3.2 Hz, 1H, ArH), 7.44–7.37 (m, 3H, ArH), 6.74–6.73 (m, 1H, ArH), 2.22 (s, 3H, CH₃); ¹³C NMR (100 MHz, DMSO-*d*₆) δ: 159.8, 158.1, 156.9, 151.1, 147.7, 146.4, 139.6, 138.7, 136.8, 133.1, 129.8 (4C), 129.1 (2C), 127.6, 122.2 (2C), 121.6 (2C), 115.8, 112.7, 105.9, 25.2; EI-MS: *m/z* = 455 [M⁺] (5.62%); Anal. Calcd. for: C₂₅H₁₈ClN₅O₂: C, 65.86; H, 3.98; N, 15.36; found C, 66.04; H, 4.13; N, 15.62.

4-Methyl-*N*-(4-(6-methyl-4-oxo-1-phenyl-1H-pyrazolo[3,4-*d*]pyrimidin-5(4*H*)-yl)phenyl)benzamide (12d). Gray solid: 55% yield; m.p. 306–308 °C; IR (KBr, cm⁻¹) 3337 (NH), 3060, 3032 (CH aromatic), 2974, 2947 (CH aliphatic), 1686, 1647 (2 C=O), 1570 (C=N), 1519 (C=C). ¹H NMR (400 MHz, DMSO-*d*₆) δ: 10.41 (s, 1H, NH, D₂O exchangeable), 8.36 (s, 1H, CH pyrazole), 8.11 (d, *J* = 7.2 Hz, 2H, ArH), 7.98 (d, *J* = 7.6 Hz, 2H, ArH), 7.90 (t, *J* = 8.8 Hz, 2H, ArH), 7.60 (t, *J* = 8.0 Hz, 2H, ArH), 7.41–7.33 (m, 5H, ArH), 2.40 (s, 3H, CH₃), 2.23 (s, 3H, CH₃); ¹³C NMR (100 MHz, DMSO-*d*₆) δ: 165.6, 160.0, 151.5, 141.9, 140.0, 138.5, 136.8, 135.4, 132.5, 129.7, 129.43, 129.35, 129.1, 128.2, 128.1, 127.5, 122.1, 121.6, 121.1 (4C), 105.0, 25.2, 21.5; EI-MS: *m/z* = 435 [M⁺] (9.77%); Anal. Calcd. for C₂₆H₂₁N₅O₂: C, 71.71; H, 4.86; N, 16.08; found C, 71.53; H, 4.97; N, 16.29.

***N*-(4-(6-Methyl-4-oxo-1-phenyl-1H-pyrazolo[3,4-*d*]pyrimidin-5(4*H*)-yl)phenyl)-4-nitrobenzamide (12e).** Gray solid: 46% yield; m.p. 298–300 °C; IR (KBr, cm⁻¹) 3306 (NH), 3101, 3062 (CH aromatic), 2924, 2858 (CH aliphatic), 1674 broad peak (2 C=O), 1597 (C=N), 1508 (C=C). ¹H NMR (400 MHz, DMSO-

d_6) δ : 10.80 (s, 1H, NH, D₂O exchangeable), 8.41 (d, J = 8.8 Hz, 2H, ArH), 8.36 (s, 1H, CH pyrazole), 8.23 (d, J = 8.8 Hz, 2H, ArH), 8.11 (d, J = 7.6 Hz, 2H, ArH), 7.98 (d, J = 8.4 Hz, 2H, ArH), 7.60 (t, J = 7.6 Hz, 2H, ArH), 7.46–7.41 (m, 3H, ArH), 2.23 (s, 3H, CH₃); ¹³C NMR (100 MHz, DMSO- d_6) δ : 164.8, 159.7, 158.2, 151.1, 149.7, 140.8, 139.6, 138.6, 136.7, 133.6, 129.75, 129.69, 129.6, 129.3, 127.6, 124.1 (2C), 122.2 (2C), 121.8 (2C), 121.4 (2C), 105.8, 25.1; EI-MS: m/z = 466 [M^+] (8.85%); Anal. Calcd. for: C₂₅H₁₈N₆O₄: C, 64.37; H, 3.89; N, 18.02; found C, 64.59; H, 4.02; N, 18.19.

Biological evaluation

The biological assays were performed according to the documented protocols, which can be found in the ESI.† The assays included antiproliferative activity screening by NCI,^{57–61} MTT assay,⁶² *in vitro* VEGFR-2 inhibitory evaluation,⁵¹ wound healing test,⁴⁹ cell cycle analysis,⁶³ apoptosis evaluation,⁶⁴ and caspase-3 enzyme evaluation.³⁰

Molecular modeling studies

The X-ray crystallographic structure of VEGFR-2 co-crystallized with sunitinib (PDB ID: 4AGD)⁶⁵ was obtained from the Protein Data Bank (PDB) (<https://www.Rcsb.Org/Structure/4AGD>). Molecular docking was conducted using the

Molecular Operating Environment software (MOE, version 2015.10). The receptor was prepared for docking using the Protonate 3D protocol in MOE with default settings. Sunitinib was initially docked to the VEGFR-2 active site to validate the docking protocol. Once the protocol was validated, the newly synthesized compounds **12a–d** were examined for their interactions with the VEGFR-2 active site, and their binding patterns were predicted. The compounds were built using the MOE builder, and their structures were energy-minimized using the MMFF94x force field. The Triangle Matcher placement method and London dG scoring function were employed for the docking process.

Results and discussion

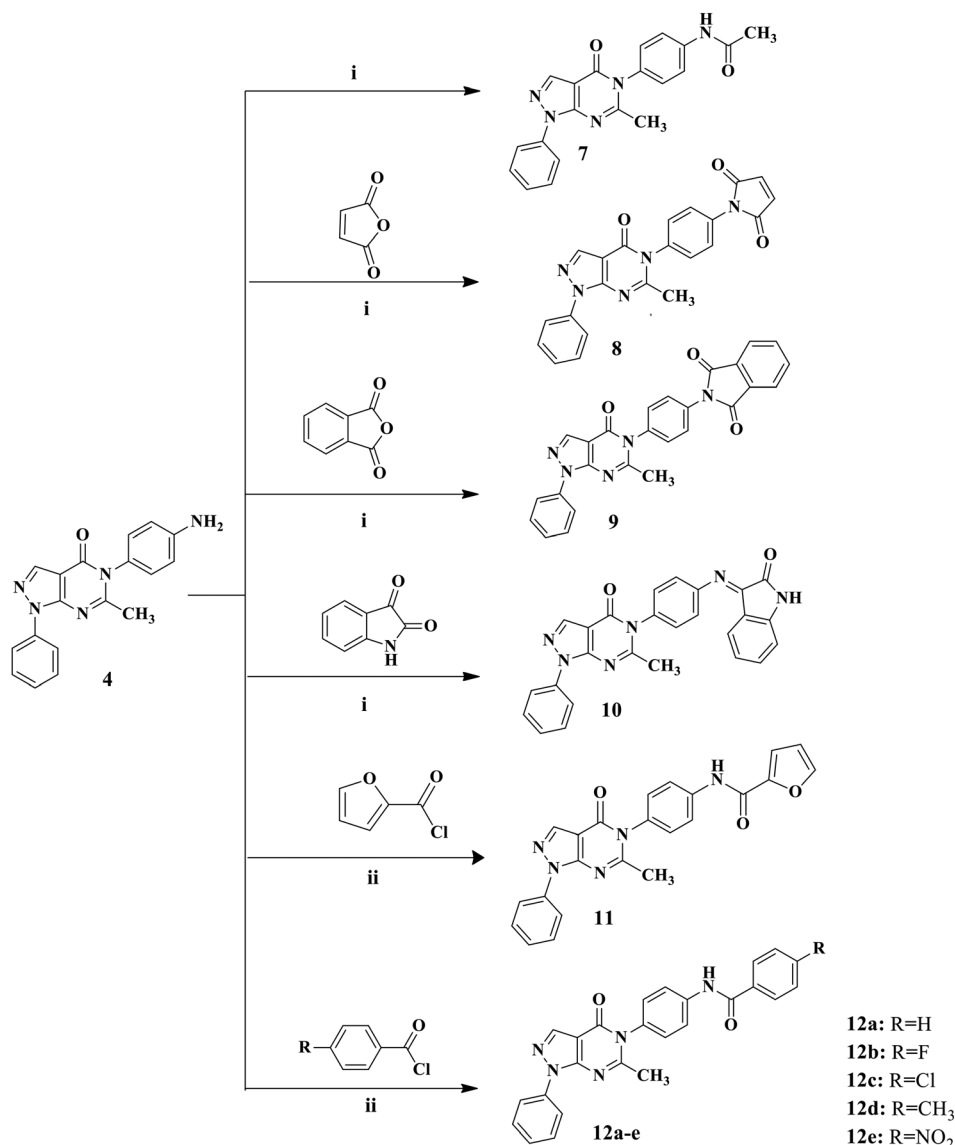
Chemistry

Twelve pyrazolo[3,4-*d*]pyrimidine derivatives were synthesized in several stages, as illustrated in Schemes 1 and 2. The newly prepared compounds were characterized by IR, ¹H NMR, ¹³C NMR, mass spectroscopy and elemental analyses. The synthesis began with the reaction of ethyl 2-cyano-3-ethoxypropanoate and phenylhydrazine in absolute ethanol, resulting in the formation of ethyl 5-amino-1-phenyl-1*H*-pyrazole-4-carboxylate (**1**).⁵⁴ Subsequent basic hydrolysis of



Reagents and conditions : i) NaOH, ethanol 95% , reflux 6 h; ii) Acetic anhydride reflux 5 h; iii) *p*-Phenylene diamine, n-butanol, reflux 8 h; iv) *p*-Amino acetophenone, n-butanol, reflux 16 h; v) 40% NaOH , *p*-Methoxy benzaldehyde, stirring 3 h.

Scheme 1 Synthetic pathways of pyrazolopyrimidine derivatives 4–6.



Scheme 2 Synthetic pathways of pyrazolopyrimidine derivatives 7–11, and 12a–e.

compound **1** yielded 5-amino-1-phenyl-1*H*-pyrazole-4-carboxylic acid (**2**),⁵⁵ which was further refluxed in acetic anhydride to obtain the key intermediate, 6-methyl-1-phenylpyrazolo[3,4-*d*][1,3]oxazin-4(1*H*)-one (**3**).⁵⁶ Compound **3** was then used in the reaction with *p*-phenylenediamine and *p*-aminoacetophenone, leading to the formation of the corresponding 5-(4-substituted phenyl)-1*H*-pyrazolo[3,4-*d*]pyrimidine-4-one derivatives, namely compounds **4** and **5**, respectively.⁵⁶ The presence of NH₂ groups in compound **4** was confirmed by the peaks observed at 3447 and 3420 cm^{−1} in the IR spectrum. In the ¹H NMR spectrum of compound **4**, a singlet signal at δ 5.44 ppm was observed, which could be attributed to the presence of an NH₂ group that underwent exchange with D₂O, indicating its presence. Furthermore, the mass spectrum of compound **4** showed

its molecular ion peak [M⁺], which also corresponds to its base peak at *m/z* 317.

Furthermore, 5-(4-(3-(4-methoxyphenyl)acryloyl)phenyl)-6-methyl-1-phenyl-1*H*-pyrazolo[3,4-*d*]pyrimidin-4(5*H*)-one (**6**) was synthesized by stirring compound **5** with *p*-methoxybenzaldehyde in the presence of NaOH. The ¹H NMR spectrum of compound **6** displayed a doublet signal at δ 7.72, indicating the presence of a (CH=CH) group with coupling constant 15.6 ppm. The coupling constant value of the enone protons confirmed the *trans* (*E*) configuration of the chalcone. Additionally, a singlet signal at δ 3.83 ppm was observed, which could be attributed to the OCH₃ group. Moreover, the mass spectrum of compound **6** displayed its molecular ion peak at *m/z* 462. Upon refluxing compound **4** with glacial acetic acid, *N*-(4-(6-methyl-4-oxo-1-phenyl-1*H*-

pyrazolo[3,4-*d*]pyrimidin-5(4*H*)-yl)phenyl)acetamide (**7**) was obtained. The IR spectrum of compound **7** exhibited a peak at 3414 cm⁻¹, indicating the presence of NH. In the ¹H NMR spectrum, a D₂O exchangeable singlet signal at δ 10.18 ppm corresponding to the NH proton was observed, along with a singlet signal at δ 2.19 ppm representing CH₃. Additionally, the mass spectrum of compound **7** showed its molecular ion peak at *m/z* 359. In contrast, compounds **8** and **9** were synthesized through the reaction of compound **4** with the corresponding acid anhydride in the presence of glacial acetic acid following a documented procedure.⁶⁶ The ¹H NMR spectra of compounds **8** and **9** were confirmed by the disappearance of the NH₂ signal present in starting compound **4** at δ 5.44 ppm. Additionally, an increase in the number of aromatic protons further supported the successful synthesis of compound **8**. Another significant piece of evidence for the synthesis of compound **8** was the emergence of signals at δ 170.2 ppm in the ¹³C NMR spectrum, indicating the presence of C=O groups. Furthermore, the mass spectrum of compound **8** exhibited its molecular ion peak, which corresponds to its base peak at *m/z* 397. Compound **9** exhibited three peaks in the IR spectrum at 1716, 1681, and 1643 cm⁻¹, along with signals at δ 168.1, 167.8, and 167.3 ppm in the ¹³C NMR spectrum, providing further confirmation of the presence of three C=O groups. Additionally, the mass spectrum of compound **9** showed its molecular ion peak at *m/z* 447. As depicted in Scheme 2, the reaction of compound **4** with isatin in the presence of glacial acetic acid resulted in the formation of hydrazone derivative **10**. The ¹H NMR spectrum of derivative **10** exhibited a singlet signal at δ 11.14 ppm, which could be attributed to the NH proton, and showed exchangeability with D₂O. Moreover, the integration of aromatic protons indicated an increase in their abundance. Analysis of the IR spectrum of derivative **10** revealed the presence of an NH group, as evidenced by a peak at 3252 cm⁻¹, and three C=O groups, indicated by peaks at 1732, 1693, and 1659 cm⁻¹. Moreover, the mass spectrum of compound **10** exhibited its molecular ion peak at *m/z* 446. Conversely, the reaction of key intermediate **4** with furoyl chloride yielded the desired compound **11**. The ¹H NMR spectrum of compound **11** confirmed the presence of a D₂O exchangeable singlet signal at δ 10.57 ppm, which corresponded to the NH proton. Additionally, evidence of the formation of compound **11** was observed in the ¹³C NMR spectrum, where the two signals at δ 165.2 and 159.7 ppm indicated the presence of two C=O groups. The IR spectrum further supports the formation of a new compound, as evidenced by the broad peak at 1685 cm⁻¹, which corresponded to the presence of two C=O groups. Additionally, the mass spectrum of compound **11** displayed [M⁺ + H] at *m/z* 412.

Compounds **12a–e** were synthesized by refluxing compound **4** with substituted benzoyl chloride, in the presence of anhydrous K₂CO₃ and dry benzene. The ¹H NMR spectra of compounds **12a–e** displayed D₂O exchangeable singlet signals in the range of δ 10.41–10.80 ppm,

corresponding to the NH group. Another confirmation of the formation of compounds **12a–e** is the increase in aromatic protons observed in their respective ¹H NMR spectra. Furthermore, the structures of compounds **12a–e** were confirmed by their ¹³C NMR spectra, which displayed signals in the range of δ 158.1–166.4 ppm, corresponding to the C=O group. Finally, the mass spectra of compounds **12a–e** exhibited their molecular ion peaks at *m/z* 421, 439, 455, 435 and 466, respectively.

Biological evaluation

Antiproliferative activity evaluation. In this study, a series of newly synthesized pyrazolopyrimidine derivatives (compounds **4**, **6–11**, and **12a–e**) was screened by the Developmental Therapeutic Program (DTP) at the National Cancer Institute (USA) to assess their anticancer properties.^{57–61} The compounds were evaluated at a concentration of 10 μ M as a single dose against a panel of 60 human tumor cell lines, including leukemia, non-small cell lung cancer, colon cancer, central nervous system (CNS) tumors, melanoma, ovarian cancer, kidney cancer, prostate cancer, and breast cancer cell lines. The antiproliferative activities of the **12** compounds are summarized in Table 1, which shows growth inhibition percentage (GI%) values reflecting their respective antiproliferative effects.

Screening conducted by the National Cancer Institute (NCI) revealed that compound **4** exhibited moderate antitumor activity against 13 cell lines, with an overall mean inhibition of 20.71%. Compound **5** reacted with *p*-methoxybenzaldehyde, leading to the formation of chalcone **6**. Chalcone **6** demonstrated a lethal effect on the leukemia cell line RPMI-8226, along with strong antiproliferative activity against leukemia K-562, colon cancer HCT-116, melanoma (MDA-MB-435 and SK-MEL-5), and breast cancer (MCF7 and MDA-MB-468) cell lines, resulting in an overall mean inhibition of 33.65%.

The acetylated derivative, compound **7**, demonstrated potent antiproliferative activity against the melanoma SK-MEL-5 and breast cancer T-47D cell lines, resulting in an overall mean inhibition of 23.39%. Conversely, compounds **8** and **9** exhibited no significant inhibitory activity, with mean inhibitions of 0.44% and 1.05%, respectively.

The isatin derivative (compound **10**) displayed a mean inhibition of 20.94% and moderate activity against 17 cancer cell lines, with inhibition ranging from 30.66% to 52.13%.

Furthermore, the furoyl derivative, compound **11**, exhibited decreased antiproliferative activity and only demonstrated moderate anticancer activity against three cell lines, leukemia K-562, breast cancer cell lines T-47D and MDA-MB-468, with a mean inhibition of 9.46%.

In contrast to compound **11**, benzoyl derivatives **12a–e** displayed increased activity, with a mean inhibition range of 31.57–39.63%. Compound **12a** exhibited strong inhibitory activity against the melanoma SK-MEL-5 cell line, as well as the breast cancer cell lines T-47D and MDA-MB-468, with

Table 1 Percentages of growth inhibition obtained from tests of compounds **4**, **6–11**, **12a–e** against a panel of tumor cell lines at a single concentration of (10 μ M)

Panel/cell lines												
Compounds	4	6	7	8	9	10	11	12a	12b	12c	12d	12e
Leukemia												
CCRF-CEM	21.04	53.62	30.83	32.21	—	37.81	23.57	49.51	65.18	25.29	53.73	52.54
HL-60(TB)	—	55.3	28.32	—	—	—	19.80	18.49	57.49	48.07	48.64	54.04
K-562	52.08	87.56	55.38	—	—	34.44	30.15	66.83	72.79	61.27	68.79	68.85
MOLT-4	—	55.26	43.58	—	—	34.13	—	68.09	94.62	30.70	65.69	63.4
RPMI-8226	48.17	>100	47.47	—	—	36.46	26.08	43.56	64.75	52.90	41.57	47.70
Non-small cell lung cancer												
A549/ATCC	—	—	—	—	—	—	—	28.89	45.01	26.15	34.23	33.03
EKVX	63.32	57.12	66.76	—	—	52.13	26.92	65.66	69.78	68.54	69.52	69.34
HOP-62	16.18	19.48	—	—	—	—	—	37.86	35.43	41.13	21.19	—
HOP-92	—	—	16.97	—	—	17.59	—	29.21	—	37.84	—	—
NCI-H226	18.04	29.42	33.45	—	—	24.73	—	44.67	43.77	49.07	45.20	50.76
NCI-H23	40.11	27.59	31.69	—	—	30.66	—	45.55	49.78	47.22	46.45	50.64
NCI-H322M	—	—	—	—	—	—	—	—	—	—	—	17.22
NCI-H460	16.76	—	—	—	—	—	—	27.93	45.65	28.81	24.63	26.41
NCI-H522	—	42.64	25.04	—	—	16.75	—	20.71	36.06	32.28	28.77	38.94
Colon Cancer												
COLO 205	—	—	—	—	—	—	—	20.17	37.69	18.80	22.64	25.92
HCC-2998	—	—	—	—	—	—	—	—	20.11	15.77	—	—
HCT-116	25.88	90.29	28.85	—	—	17.88	—	41.89	51.66	44.53	48.49	55.63
HCT-15	—	46.48	15.14	—	—	15.65	—	20.24	33.94	23.21	24.65	28.57
HT29	—	28.51	—	—	—	—	—	25.19	36.52	28.04	28.83	21.55
KM12	—	68.43	—	—	—	—	—	24.72	35.89	19.25	22.48	20.44
SW-620	—	24.86	—	—	—	—	—	—	23.50	17.33	—	—
CNS Cancer												
SF-268	17.43	—	—	—	—	—	—	21.49	—	—	—	—
SF-295	27.07	34.45	36.45	—	—	24.74	15.35	46.55	60.44	45.85	49.36	56.31
SF-539	19.39	22.44	18.95	—	—	20.95	—	19.79	—	—	18.65	18.68
SNB-19	—	18.23	16.43	—	—	36.04	—	23.64	19.63	16.28	17.93	25.41
SNB-75	28.10	—	—	—	—	—	—	43.20	35.47	27.47	17.25	32.88
U251	—	25.89	—	—	—	39.63	—	—	18.89	—	—	—
Melanoma												
LOX IMVI	18.48	56.05	21.15	—	—	18.26	—	26.77	38.21	33.44	32.84	34.09
MALME-3M	17.83	39.45	22.27	—	—	23.07	16.63	29.80	31.56	33.30	32.32	33.98
M14	—	46.93	—	—	—	18.76	—	23.60	37.10	24.55	26.77	24.65
MDA-MB-435	22.95	88.84	21.14	—	—	—	—	27.23	46.24	30.21	29.45	33.64
SK-MEL-2	17.82	29.37	24.32	—	—	—	—	—	22.12	26.05	21.66	29.33
SK-MEL-28	—	—	—	—	—	—	—	—	16.22	17.05	19.33	18.2
SK-MEL-5	66.85	72.33	77.39	—	—	42.92	23.07	76.15	>100	80.35	92.95	82.37
UACC-257	34.27	25.36	41.66	—	—	29.34	—	46.94	68.16	53.87	57.98	50.77
UACC-62	34.55	49.98	38.28	—	—	36.16	16.55	36.84	36.89	32.25	39.24	39.64
Ovarian Cancer												
IGROV1	15.00	—	—	—	—	34.67	—	—	26.50	21.34	28.41	31.06
OVCAR-3	—	38.96	—	—	—	24.31	—	16.81	—	17.45	—	—
OVCAR-4	48.74	34.28	44.83	—	—	43.94	21.16	53.18	59.89	53.9	50.21	48.22
OVCAR-5	—	—	—	—	—	—	—	—	—	—	—	—
OVCAR-8	—	16.55	20.03	—	—	24.77	—	38.40	36.29	43.44	23.2	34.15
NCI/ADR-RES	—	37.65	—	—	—	—	—	30.38	57.22	44.50	47.31	47.21
SK-OV-3	—	—	—	—	—	19.63	—	19.01	—	—	—	—
Renal Cancer												
786-0	—	15.44	—	—	—	—	—	20.37	17.49	20.30	—	16.29
A498	16.77	—	16.13	—	—	—	—	—	—	—	—	19.56
ACHN	27.07	29.04	29.80	—	—	27.71	—	36.66	39.02	32.64	38.25	39.61
CAKI-1	31.71	25.01	31.09	—	—	31.69	—	33.41	34.29	29.71	27.56	31.49
RXF 393	—	15.63	—	—	—	28.96	—	18.94	20.95	—	—	26.37
SN12C	21.06	18.43	26.06	—	—	37.33	—	24.32	25.59	17.01	26.66	28.96
TK-10	21.82	—	20.38	—	—	—	—	18.56	28.96	19.85	17.71	31.47
Prostate Cancer												
PC-3	17.99	34.93	30.34	—	—	24.01	—	29.52	46.89	36.72	28.35	33.7
DU-145	17.28	16.81	17.82	—	—	—	—	18.59	19.29	17.78	15.14	21.02
Breast Cancer												
MCF7	37.65	91.70	44.36	—	—	33.68	23.40	47.09	64.15	46.75	52.21	56.70
HS 578T	21.44	—	—	—	—	17.60	—	28.95	21.28	20.05	15.17	23.14
BT-549	31.16	55.01	48.01	—	—	22.15	—	39.07	54.03	35.98	40.84	48.8

Table 1 (continued)

Panel/cell lines	4	6	7	8	9	10	11	12a	12b	12c	12d	12e
Compounds	4	6	7	8	9	10	11	12a	12b	12c	12d	12e
T-47D	64.88	65.3	70.86	—	—	38.28	34.05	72.41	81.97	72.47	65.39	66.48
MDA-MB-468	62.38	88.68	64.22	18.65	—	51.42	37.27	71.01	85.50	84.33	78.94	68.64
Mean inhibition	20.71	33.65	23.39	0.44	1.05	20.94	9.46	31.57	39.63	32.42	31.99	34.14

Blank entries (—) indicate weak growth inhibition of less than 15%; entries in bold indicate strong growth inhibition (GI% > 70%).

growth inhibition percentages (GI%) of 76.15%, 72.41%, and 71.01%, respectively. Additionally, it demonstrated moderate anticancer activity against 20 cancer cell lines with a mean inhibition of 31.57%.

The *p*-fluorobenzoyl derivative compound **12b** showed a lethal effect on the melanoma cell line SK-MEL-5, along with strong anticancer activity against the leukemia cell lines K-562 and MOLT-4, with GI% values of 72.79% and 94.62%, respectively. It also exhibited strong anticancer activity against breast cancer cell lines T-47D and MDA-MB-468, with GI% values of 81.97% and 85.50%, respectively. Furthermore, compound **12b** exhibited moderate anticancer activity against 31 cancer cell lines and recorded the highest mean inhibition among all the tested compounds, with a score of 39.63%.

When the *p*-fluoro group was substituted with a *p*-chloro group, as in compound **12c**, strong antitumor activity was observed against three cell lines: melanoma SK-MEL-5 with a GI% of 80.35% and breast cancer cell lines T-47D and MDA-MB-468 with GI% values of 72.47% and 84.33%, respectively.

Additionally, it displayed moderate anticancer activity against 24 cell lines, with GI% ranging from 30.70% to 68.54%. The *p*-methyl benzoyl derivative **12d** demonstrated a decrease in antiproliferative activity compared to **12c**, exhibiting only strong antitumor activity against two cell lines namely melanoma SK-MEL-5 and breast cancer MDA-MB-468, with growth inhibition of 92.95 and 78.94%, respectively. In addition, compound **12d** demonstrated moderate anticancer activity against 21 cell lines, with a GI range of 32.32–69.52%. Altering the *p*-methyl group with a *p*-nitro group led to the formation of compound **12e**, which showed strong antitumor activity only against the melanoma SK-MEL-5 cell line with a growth inhibition of 82.37%, together with moderate activity against several cell lines of different types of cancer with growth inhibition ranging from 31.06–69.34%.

Among the newly synthesized derivatives with varying structures and antiproliferative activities, compounds containing amide spacers (**12a–e**) exhibited higher anticancer activities than those with an azomethine spacer (**10**) or compounds directly attached without spacers (**8** and **9**).

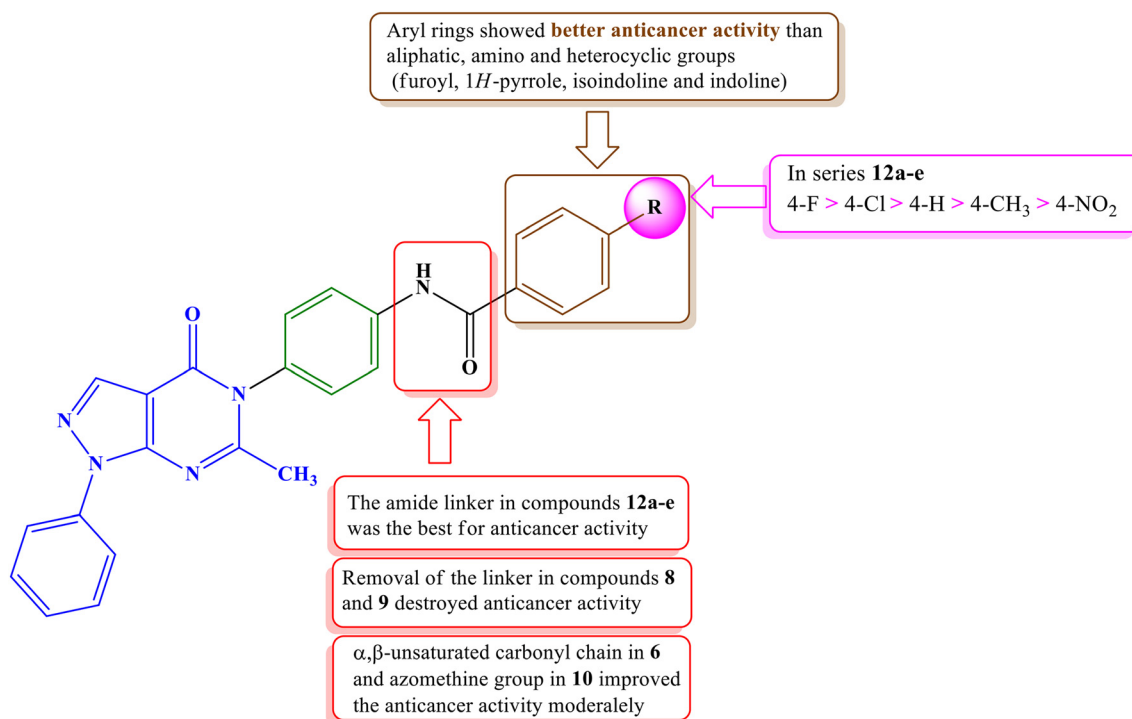


Fig. 4 Structure–activity relationship of the pyrazolo[3,4-*d*]pyrimidine synthesized compounds.

Table 2 *In vitro* cytotoxicity IC₅₀ of compounds **12a–d** against breast cancer cell lines MDA-MB-468, T47D, and normal cell line MCF-10a compared to staurosporine

Codes	Cytotoxicity IC ₅₀ μM			Selectivity index	
	MCF-10a	MDA-MB-468	T47D	MDA-MB-468	T47D
12a	55.48 ± 2.37	27.02 ± 1.02	35.511 ± 1.58	2.05	1.56
12b	22.77 ± 0.97	3.343 ± 0.13	4.792 ± 0.21	6.81	4.75
12c	34.57 ± 1.48	10.661 ± 0.4	20.11 ± 0.9	3.24	1.72
12d	58.18 ± 2.49	16.030 ± 0.6	NT ^a	3.63	NT ^a
Staurosporine	18.01 ± 0.77	6.358 ± 0.24	4.849 ± 0.22	2.83	3.71

^a Not tested.

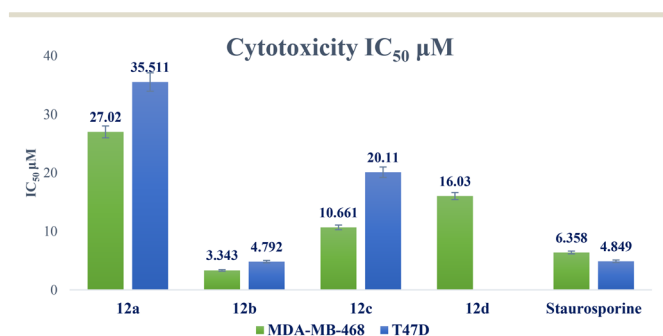
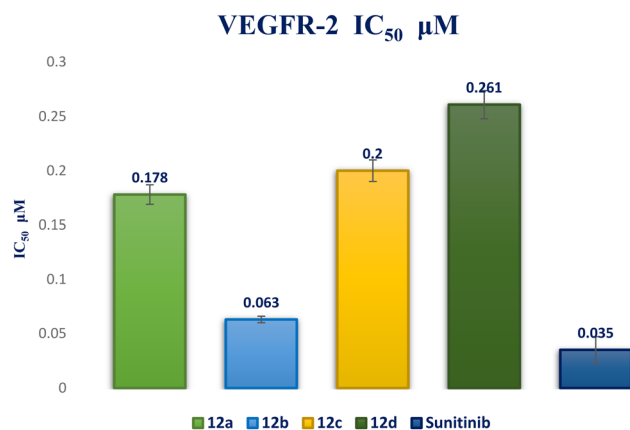
Notably, the presence of a 4-substituted phenyl group (**12a–e**) in the terminal hydrophobic region demonstrated the most potent anticancer activity, surpassing compounds with an amino group (**4**), methyl group (**7**), or various heterocyclic rings, such as 1-*H*-pyrrole (**8**), isoindoline (**9**), indoline (**10**), and furoyl (**11**).

Among the most active series (**12a–e**), compound **12b**, featuring a 4-fluorophenyl group, exhibited the highest potency, followed by the 4-chlorophenyl derivative **12c**. Conversely, compound **12e**, which was substituted with a strongly electron-withdrawing nitro group, displayed the lowest activity. The SAR of the synthesized compounds is summarized in Fig. 4.

MTT assay and selectivity index (SI) calculation. A preliminary study was conducted to determine the antiproliferative activities of compounds **12a–d**. The screening involved testing compounds **12a–c** against two breast cancer cell lines, MDA-MB-468 and T47D, and compound **12d** was specifically examined against the breast cell line MDA-MB-468. Mosmann's MTT colorimetric assay protocol was employed.⁶² Staurosporine, a reference cytotoxic drug, was used in all experiments. The growth inhibitory concentration (IC₅₀) was calculated based on the results obtained. These values represent the concentration required to inhibit 50% of cell growth after 72 h. As shown in Table 2 and Fig. 5, the IC₅₀ values were computed based on the concentration–inhibition response curves. In cytotoxicity studies, compound **12b** exhibited the most significant effect on MDA-MB-468 and T47D breast cancer cell lines, followed by compound **12c** with IC₅₀ values of (3.343 ± 0.13 and 4.792

± 0.21 μM) and (10.661 ± 0.4 and 20.11 ± 0.9 μM) for **12b** and **12c**, respectively. In comparison, the IC₅₀ values of staurosporine were 6.358 ± 0.24 and 4.849 ± 0.22 μM for the corresponding cell lines. Compounds **12a** and **12d** exhibited weak activity against MDA-MB-468 cells, with IC₅₀ values of 27.02 ± 1.02 and 16.030 ± 0.6 μM, respectively. Furthermore, compound **12a** demonstrated weak anticancer activity against the T47D cell line, with an IC₅₀ value of 35.511 ± 1.58 μM. Additionally, it is critical to consider the undesirable side effects of chemotherapeutic agents on normal cells, which can be attributed to their non-selective cytotoxicity. Therefore, we evaluated the impact of the most promising compounds **12a–d** on the human mammary epithelial cell line (MCF-10a) as a representative of normal breast cells. The results of the selectivity index (SI) assessment of derivatives **12a–d** against normal cells are presented in Table 2. SI was determined by comparing the cytotoxicity (IC₅₀) of the normal breast cell line (MCF-10a) with that of breast cancer cell lines (MDA-MB-468 and T47D). The findings demonstrated that compound **12b** exhibited the highest selectivity towards breast cancer cells MDA-MB-468 and T47D, with an IC₅₀ value of 22.77 ± 0.97 μM and SI values of 6.81 and 4.75, respectively. In comparison, staurosporine yielded an IC₅₀ value of 18.01 ± 0.77 μM and SI values of 2.83 and 3.71 for the corresponding cell lines.

Assessment of VEGFR-2 inhibitory activity. Based on the promising antiproliferative activity exhibited by the four most

**Fig. 5** Graphical illustration of IC₅₀ of compounds **12a–d** against breast cancer cell lines compared to staurosporine.**Fig. 6** IC₅₀ bar graph for compounds **12a–d** against VEGFR-2 in comparison to sunitinib.

potent derivatives **12a–d**, further evaluation was conducted to assess their effects on VEGFR-2 inhibition. Sunitinib was used as a positive control in this experiment. Fig. 6 shows the 50% inhibitory concentration (IC_{50}) calculated based on the concentration–inhibition response curve. Compared to sunitinib ($IC_{50} = 0.035 \pm 0.012 \mu\text{M}$), compounds **12a–d** demonstrated VEGFR-2 inhibitory activity with IC_{50} values of 0.178 ± 0.009 , 0.063 ± 0.003 , 0.20 ± 0.01 , and $0.261 \pm 0.013 \mu\text{M}$, respectively. Notably, compound **12b** displayed potent inhibition of VEGFR-2, indicating its potential as a promising inhibitor, with significant antiproliferative properties.

Wound healing test. Angiogenesis plays a key role in wound healing. It involves the formation of new blood vessels that supply nutrients and oxygen to developing tissues, leading to the formation of provisional granulation tissue. An *in vitro* wound-healing test was conducted to evaluate the antiangiogenic activity of compound **12b**. The results of the wound closure study indicated that the percentage of wound closure in the compound **12b** group was 75.555 ± 4.11 , while

in the sunitinib group, it was 57.777 ± 3.15 . The control group exhibited a wound closure rate of 98.518 ± 5.36 . Notably, compounds **12b** and sunitinib significantly reduced the propagation and migration potential of human umbilical vein endothelial cells (HUVECs) compared with the control group after 72 h. This reduction resulted in a decreased healing rate of 23% and 41%, respectively, compared to the control (Fig. 7).

Cell cycle analysis. As part of the drug discovery process, it is essential to find a stage of cell arrest that is likely to occur within a cell.⁶⁷ By going through successive cell cycles, eukaryotic cells can replicate themselves. The action of any antiproliferative drug is to stop the growth of targeted cells at one or more growth checkpoints (phases). As a result of persistent cell damage, checkpoint signaling may prompt several systems to initiate the process of apoptosis. In this study, the cell cycle distribution of the breast cancer MDA-MB-468 cell line was determined by DNA flow cytometry analysis. Fig. 8 shows the phases of the cell population after

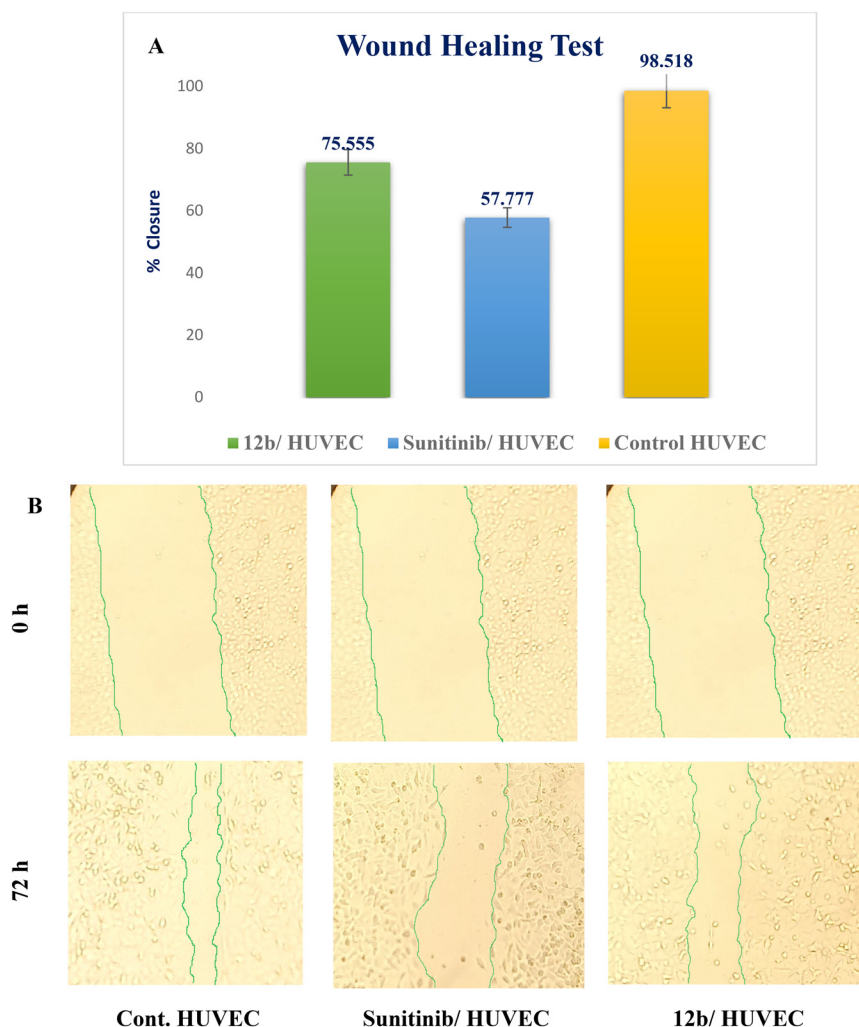


Fig. 7 Effect of sunitinib and compound **12b** on endothelial cell migration in HUVEC cells. A) The following graph illustrates the percentage of wound closure for control and treated cells; B) a 72 h study using compound **12b** and sunitinib was conducted on HUVECs. Values are expressed as mean \pm standard deviation.



Fig. 8 Cell cycle arrest is caused by compound **12b** in MDA-MB-468 cells. A) Control MDA-MB-468; B) cells treated with **12b**; C) the diagram illustrates the distribution of cell cycle phases in control and treated cells.

incubation with compound **12b** at its IC_{50} (3.343 μ M) for 24 h. Compound **12b** showed an increase in the proportion of cells in the S phase by 1.53-fold compared to the control (DMSO). In addition, the cell population decreased by 10.43% and 43.46% in the G0-G1 phase and the G2/M phase, respectively. The results indicate that compound **12b** induces arrest of the cell cycle in MDA-MB-468 cells at the S phase and decreases cellular proliferation.

Evaluation of apoptosis by annexin V. In this study, a dual-staining assay employing annexin V/propidium iodide (PI)^{68,69} was used to examine the effect of compound **12b** on cell apoptosis. An apoptosis assay was performed on MDA-MB-468 breast cancer cells before and after treatment with compound **12b**. The findings revealed that compound **12b** induced a significant increase in annexin V apoptotic cells during both the early (from 0.52% to 15.85%) and late apoptotic stages (from 0.17% to 22.49%) (Table 3 and Fig. 9). Furthermore, compound **12b** resulted in an 18.98-fold increase in total apoptosis compared to that in the control (DMSO).

Effect of compound **12b on the caspase-3 level.** Inhibitors targeting VEGFR-2 tyrosine kinase have been widely

recognized for their capacity to enhance the intrinsic apoptotic pathway by upregulating caspase-3 activity in various cell types.^{70,71} Consequently, the most potent compound, **12b**, was selected to evaluate its potential to induce apoptosis in MDA-MB-468 breast cancer cells using a caspase-3 assay. For comparison, sunitinib was used as a positive control. As shown in Fig. 10, compound **12b** exhibited a 7.32-fold increase in caspase-3 levels, whereas sunitinib showed a significantly higher increase of 10.35-fold. Based on the proposed mechanism of action of compound **12b**, we hypothesized that apoptosis may be induced through a caspase-dependent pathway.

Molecular docking at the active site of VEGFR-2. Molecular docking studies were conducted using Molecular Operating

Table 3 Apoptotic cell distribution in MDA-MB-468 breast cells treated with compound **12b**

Compound	Apoptosis			Necrosis
	Total	Early	Late	
12b/MDA-MB-468	43.28	15.85	22.49	4.94
Cont. MDA-MB-468	2.28	0.52	0.17	1.59



Fig. 9 The effect of compound **12b** on annexin V staining in MDA-MB-468 cells. A) Control MDA-MB-468; B) cells treated with **12b**; C) graph displaying the percentage of apoptotic and necrotic cells in control and **12b**-treated cells.

Environment (MOE) 2015.10 software to investigate the binding properties of newly synthesized compounds within

the binding site of VEGFR-2. The crystallographic structure of VEGFR-2 in its active (DFG-in) conformation (PDB ID: 4AGD) was obtained from the Protein Data Bank (PDB) (<https://www.Rcsb.Org/Structure/4AGD>).⁶⁵ In the downloaded structure, sunitinib, a type I protein kinase inhibitor, was co-crystallized with the protein. As an initial step in validating the molecular docking protocol, the co-crystallized ligand sunitinib was re-docked into the VEGFR-2 binding site. The re-docking simulation of sunitinib yielded a binding pattern at the VEGFR-2 binding site that closely resembled that of the co-crystallized ligand, with an energy score of $-8.4031 \text{ kcal mol}^{-1}$ and an RMSD of 1.2968 \AA between the docked pose and the co-crystallized ligand. Furthermore, all critical interactions observed between the co-crystallized ligand and the binding site hotspots in VEGFR-2 (Glu917, Cys919) were successfully reproduced (Fig. 11). These results from the validation step demonstrated the reliability and appropriateness of the docking protocol employed for molecular docking analysis of the newly synthesized compounds within the binding site of VEGFR-2 (Table 4).

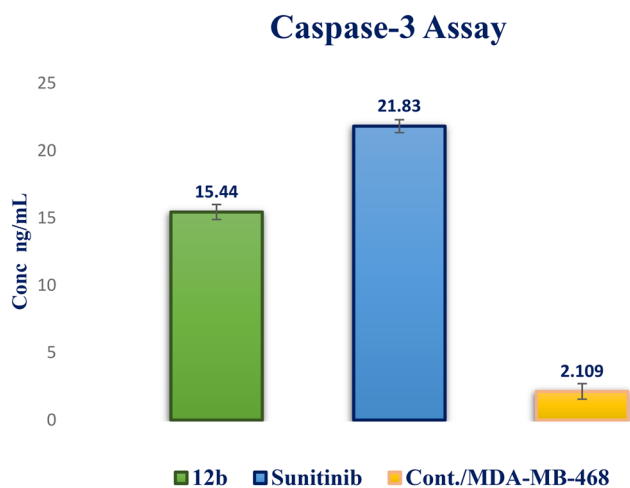


Fig. 10 Caspase-3 activity in MDA-MB-468 cells of compound **12b** compared to sunitinib.



Fig. 11 (A) Sunitinib in the VEGFR-2 active site (2D interaction diagram); (B) the superimposition of the co-crystallized sunitinib (red) and its docking poses (green) in the VEGFR-2 active site (3D representation).

Interaction analysis of the highly active designed compounds **12a–d** with crucial amino acids in the VEGFR-2 binding site indicated favorable binding outcomes overall. These compounds exhibited a good fit within the binding region of the enzyme and formed strong binding interactions, as evidenced by the 2D and 3D

representations of the docked poses. Specifically, compound **12b** demonstrated a binding pattern in the VEGFR-2 binding site that closely resembled that of sunitinib, along with a predicted docking energy of -7.6497 kcal mol $^{-1}$ (Fig. 12). In the active “DFG-in” conformation, the N2 of the pyrazolopyrimidinone ring within compound **12b**

Table 4 Table illustrating the docking energy scores (S) in kcal mol $^{-1}$, the amino acids, and their types of interaction, in addition to the distance of the active compounds **12a–d** and sunitinib within the VEGFR-2 active site

Compound	S (kcal mol $^{-1}$)	Amino acids	Types of interactions	Distance (Å)
12a	-6.4953	Asp1046	HB donor	3.15
		Cys919	HB acceptor	2.96
		Lys868	HB acceptor	3.10
		Phe1047	H-π	4.06
		Leu840	π-H	4.21
		Leu840	π-H	3.98
		Leu840	π-H	3.84
		Val848	π-H	4.36
12b	-7.6497	Cys919	HB acceptor	3.46
		Leu840	π-H	3.71
		Leu840	π-H	3.88
		Val848	π-H	4.12
		Val848	π-H	4.42
12c	-5.8195	Cys919	HB acceptor	3.03
		Leu840	π-H	4.28
		Leu840	π-H	4.29
		Leu840	π-H	3.89
12d	-5.8969	Glu885	HB donor	3.15
		Cys919	HB acceptor	3.03
		Leu840	π-H	4.29
		Leu840	π-H	4.30
		Leu840	π-H	3.89
Sunitinib	-8.4031	Asp1046	π-H	4.52
		Glu917	HB donor	3.04
		Cys919	HB acceptor	2.97
		Phe1047	H-π	4.08
		Leu840	π-H	4.00
		Val848	π-H	4.31
		Gly922	π-H	3.56

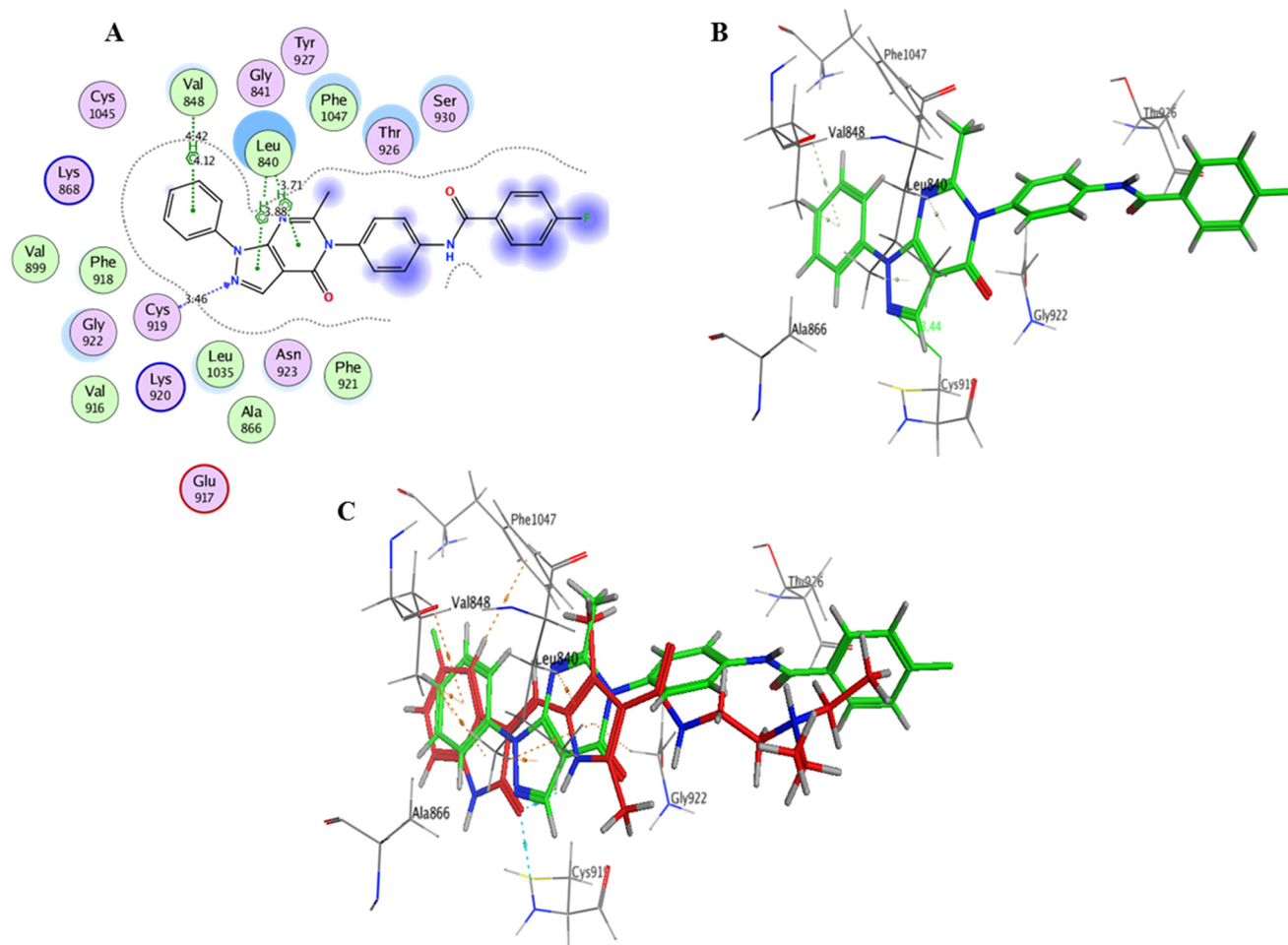


Fig. 12 A) Compound **12b** within the VEGFR-2 binding site (2D interactions); B) compound **12b** within the VEGFR-2 binding site (3D representation); C) superimposition of compound **12b** (green) with sunitinib (red) interactions within the VEGFR-2 binding site (3D representation).

formed a hydrogen bond with Cys919 in the ATP-binding pocket of VEGFR-2. Additionally, the pyrazole and pyrimidinone rings establish π -H bonds with Leu840. Furthermore, the N1-phenyl ring of the compound interacts with Val848 through two π -H bonds. Conversely, the hydrophobic 4-fluorophenyl ring of the compound fitted into an allosteric hydrophobic pocket. The docking poses of compounds **12a**, **12c**, and **12d** are shown in Fig. S1–S3 of the ESI.†

Conclusion

In this study, a novel series of pyrazolo[3,4-*d*]pyrimidine compounds, specifically **4**, **6–11**, and **12a–e**, was synthesized and evaluated for their cytotoxic effects. Among these compounds, the most active, namely **12a–d**, demonstrated significant anticancer activity against breast cancer cell lines MDA-MB-468 and T-47D. Notably, compound **12b** exhibited the highest antitumor potency against both MDA-MB-468 and T-47D cell lines, with IC_{50} values of $3.343 \pm 0.13 \mu\text{M}$ and $4.792 \pm 0.21 \mu\text{M}$, respectively. Furthermore, compound **12b** emerged as the most potent VEGFR-2 inhibitor, with an

IC_{50} value of $0.063 \pm 0.003 \mu\text{M}$, surpassing that of sunitinib ($IC_{50} = 0.035 \pm 0.012 \mu\text{M}$). These findings provide additional support for molecular docking results. Compound **12b** significantly reduced wound healing by 23%. Further analysis of the cell cycle and apoptosis demonstrated that compound **12b** induced a substantial increase in total apoptosis and arrested the cell cycle in the S phase in the MDA-MB-468 cell line. Moreover, compound **12b** induced a 7.32-fold increase in the expression of apoptotic caspase-3. Based on these findings, compound **12b** showed significant promise as a candidate for further research to develop more potent anticancer drugs.

Conflicts of interest

The authors declare no conflicts of interest.

Acknowledgements

The authors would like to thank the National Institutes of Health, USA, for their support in conducting the antiproliferative screening in this study. Additionally, the

authors acknowledge the Confirmatory Diagnostic Unit of VACSERA-EGYPT for their contribution to performing the biological assays.

References

- 1 S. C. Parija, *Pondicherry J. Nurs.*, 2022, **15**, 1–2.
- 2 J. Ferlay, M. Colombet, I. Soerjomataram, D. M. Parkin, M. Piñeros, A. Znaor and F. Bray, *Int. J. Cancer*, 2021, **149**, 778–789.
- 3 B. S. Chhikara and K. Parang, *Chem. Biol. Lett.*, 2023, **10**, 451.
- 4 D. J. Baillache and A. Unciti-Broceta, *RSC Med. Chem.*, 2020, **11**, 1112–1135.
- 5 N. M. Saleh, M. G. El-Gazzar, H. M. Aly and R. A. Othman, *Front. Chem.*, 2020, **7**, 917.
- 6 A. A. Gaber, A. H. Bayoumi, A. M. El-morsy, F. F. Sherbiny, A. B. M. Mehany and I. H. Eissa, *Bioorg. Chem.*, 2018, **80**, 375–395.
- 7 N. S. Abdou, R. A. T. Serya, A. Esmat, M. F. Tolba, N. S. M. Ismail and K. A. M. Abouzid, *MedChemComm*, 2015, **6**, 1518–1534.
- 8 M. Kim, M. Baek and D. J. Kim, *Curr. Pharm. Des.*, 2017, **23**, 4226–4246.
- 9 M. A. Abdelgawad, R. B. Bakr, O. A. Alkhoja and W. R. Mohamed, *Bioorg. Chem.*, 2016, **66**, 88–96.
- 10 C. Wang, H. Liu, Z. Song, Y. Ji, L. Xing, X. Peng, X. Wang, J. Ai, M. Geng and A. Zhang, *Bioorg. Med. Chem. Lett.*, 2017, **27**, 2544–2548.
- 11 S. J. Modi and V. M. Kulkarni, *Med. Drug Discovery*, 2019, **2**, 100009.
- 12 K. M. Cook and W. D. Figg, *Ca-Cancer J. Clin.*, 2010, **60**, 222–243.
- 13 N. Ferrara, in *Tumor Angiogenesis*, Springer International Publishing, Cham, 2019, pp. 211–226.
- 14 Z. Zhao, H. Wu, L. Wang, Y. Liu, S. Knapp, Q. Liu and N. S. Gray, *ACS Chem. Biol.*, 2014, **9**, 1230–1241.
- 15 H. Zhang, F. Gong, H. Fei, C. Li, C. Zhang, Y. Wang, Y. Xu, R. Hu and L. Sun, *Eur. J. Med. Chem.*, 2016, **109**, 371–379.
- 16 S. Sun, J. Zhang, N. Wang, X. Kong, F. Fu, H. Wang and J. Yao, *Molecules*, 2018, **23**, 24–37.
- 17 W. M. Eldehna, S. M. Abou-Seri, A. M. El Kerdawy, R. R. Ayyad, A. M. Hamdy, H. A. Ghabbour, M. M. Ali and D. A. A. El Ella, *Eur. J. Med. Chem.*, 2016, **113**, 50–62.
- 18 Z. Hao and I. Sadek, *OncoTargets Ther.*, 2016, **9**, 5495–5505.
- 19 G. Gadaleta-Caldarola, S. Infusino, R. Divella, E. Ferraro, A. Mazzocca, F. De Rose, G. Filippelli, I. Abbate and M. Brandi, *Future Oncol.*, 2015, **11**, 1863–1880.
- 20 P. Wu, T. E. Nielsen and M. H. Clausen, *Trends Pharmacol. Sci.*, 2015, **36**, 422–439.
- 21 H. K. Mahmoud, T. A. Farghaly, H. G. Abdulwahab, N. T. Al-Qurashi and M. R. Shaaban, *Eur. J. Med. Chem.*, 2020, **208**, 112752.
- 22 R. Roskoski, *Biochem. Biophys. Res. Commun.*, 2007, **356**, 323–328.
- 23 E. B. Elkaeed, R. G. Yousef, H. Elkady, I. M. M. Gobaara, B. A. Alsouk, D. Z. Husein, I. M. Ibrahim, A. M. Metwaly and I. H. Eissa, *Molecules*, 2022, **27**, 4606.
- 24 A. E. Abdallah, R. R. Mabrouk, M. M. S. Al Ward, S. I. Eissa, E. B. Elkaeed, A. B. M. Mehany, M. A. Abo-Saif, O. A. El-Feky, M. S. Alesawy and M. A. El-Zahabi, *J. Enzyme Inhib. Med. Chem.*, 2022, **37**, 573–591.
- 25 H. Elkady, A. Elwan, H. A. El-Mahdy, A. S. Doghish, A. Ismail, M. S. Taghour, E. B. Elkaeed, I. H. Eissa, M. A. Dahab, H. A. Mahdy and M. M. Khalifa, *J. Enzyme Inhib. Med. Chem.*, 2022, **37**, 397–410.
- 26 Y. Y. Wang, F. Z. Xu, Y. Y. Zhu, B. Song, D. Luo, G. Yu, S. Chen, W. Xue and J. Wu, *Bioorg. Med. Chem. Lett.*, 2018, **28**, 2979–2984.
- 27 M. Abdel-Megid, *Synth. Commun.*, 2020, **50**, 3563–3591.
- 28 A. A. Gaber, A. M. El-Morsy, F. F. Sherbiny, A. H. Bayoumi, K. M. El-Gamal, K. El-Adl, A. A. Al-Karmalawy, R. R. Ezz Eldin, M. A. Saleh and H. S. Abulkhair, *Arch. Pharm.*, 2021, e2100258.
- 29 Z. Ruzi, K. Bozorov, L. Nie, J. Zhao and H. A. Aisa, *Biomed. Pharmacother.*, 2022, **156**, 113948.
- 30 M. Maher, A. E. Kassab, A. F. Zaher and Z. Mahmoud, *J. Enzyme Inhib. Med. Chem.*, 2019, **34**, 532–546.
- 31 D. C. Kim, Y. R. Lee, B. S. Yang, K. J. Shin, D. J. Kim, B. Y. Chung and K. H. Yoo, *Eur. J. Med. Chem.*, 2003, **38**, 525–532.
- 32 S. Cherukupalli, B. Chandrasekaran, R. R. Aleti, N. Sayyad, G. A. Hampannavar, S. R. Merugu, H. R. Rachamalla, R. Banerjee and R. Karpoomath, *J. Mol. Struct.*, 2019, **1176**, 538–551.
- 33 A. A. Mandour, I. F. Nassar, M. T. A. Aal, M. A. E. Shahin, W. A. El-Sayed, M. Hegazy, A. M. Yehia, A. Ismail, M. Hagra, E. B. Elkaeed, H. M. Refaat and N. S. M. Ismail, *J. Enzyme Inhib. Med. Chem.*, 2022, **37**, 1957–1973.
- 34 F. F. Sherbiny, A. H. Bayoumi, A. M. El-Morsy, M. Sobhy and M. Hagra, *Bioorg. Chem.*, 2021, **116**, 105325.
- 35 H. K. Park, H. Jeong, E. Ko, G. Lee, J. E. Lee, S. K. Lee, A. J. Lee, J. Y. Im, S. Hu, S. H. Kim, J. H. Lee, C. Lee, S. Kang and B. H. Kang, *J. Med. Chem.*, 2017, **60**, 7569–7578.
- 36 G. S. Hassan, H. H. Kadry, S. M. Abou-Seri, M. M. Ali and A. E. E. D. Mahmoud, *Bioorg. Med. Chem.*, 2011, **19**, 6808–6817.
- 37 B. C. Huddle, E. Grimley, C. D. Buchman, M. Chtcherbinine, B. Debnath, P. Mehta, K. Yang, C. A. Morgan, S. Li, J. Felton, D. Sun, G. Mehta, N. Neamati, R. J. Buckanovich, T. D. Hurley and S. D. Larsen, *J. Med. Chem.*, 2018, **61**, 8754–8773.
- 38 M. M. Ghorab, F. A. Ragab, S. I. Alqasoumi, A. M. Alafeefy and S. A. Aboulmagd, *Eur. J. Med. Chem.*, 2010, **45**, 171–178.
- 39 A. E. Kassab, Y. El-Dash and E. M. Gedawy, *Arch. Pharm.*, 2020, **353**, e1900319.
- 40 A. Sonousi, R. A. Hassan, E. O. Osman, A. M. Abdou and S. H. Emam, *J. Enzyme Inhib. Med. Chem.*, 2022, **37**, 2644–2659.
- 41 P. A. Halim, R. A. Hassan, K. O. Mohamed, S. O. Hassanin, M. G. Khalil, A. M. Abdou and E. O. Osman, *J. Enzyme Inhib. Med. Chem.*, 2022, **37**, 189–201.

- 42 A. El-Malah, Z. Mahmoud, H. Hamed Salem, A. M. Abdou, M. M. H. Soliman and R. A. Hassan, *Green Chem. Lett. Rev.*, 2021, **14**, 220–232.
- 43 R. A. Hassan, S. H. Emam, D. Hwang, G.-D. Kim, S. O. Hassanin, M. G. Khalil, A. M. Abdou and A. Sonousi, *Bioorg. Chem.*, 2022, **118**, 105487.
- 44 A. A. Helwa, N. M. El-Dydamony, R. A. Radwan, S. M. Abdelraouf and R. M. Abdelnaby, *Bioorg. Chem.*, 2020, **102**, 104051.
- 45 N. M. El-Dydamony, R. M. Abdelnaby, R. Abdelhady, O. Ali, M. I. Fahmy, R. R. F. Eldeen and A. A. Helwa, *J. Enzyme Inhib. Med. Chem.*, 2022, **37**, 895–911.
- 46 E. O. Osman, S. H. Emam, A. Sonousi, M. M. Kandil, A. M. Abdou and R. A. Hassan, *Drug Dev. Res.*, 2023, **84**, 888–906.
- 47 M. T. M. Sayed, P. A. Halim, A. K. El Ansary and R. A. Hassan, *Drug Dev. Res.*, 2023, **84**, 1299–1319.
- 48 L. M. A. Abdel Ghany, N. M. El-Dydamony, A. A. Helwa, S. M. Abdelraouf and R. M. Abdelnaby, *New J. Chem.*, 2022, **46**, 17394–17409.
- 49 A. E. Kassab, E. M. Gedawy, M. I. A. Hamed, A. S. Doghish and R. A. Hassan, *J. Enzyme Inhib. Med. Chem.*, 2021, **36**, 922–939.
- 50 R. A. Hassan, M. I. A. Hamed, A. M. Abdou and Y. El-Dash, *Bioorg. Chem.*, 2022, **125**, 105861.
- 51 Y. El-Dash, E. Elzayat, A. M. Abdou and R. A. Hassan, *Bioorg. Chem.*, 2021, **114**, 105137.
- 52 S. H. Emam, R. A. Hassan, E. O. Osman, M. I. A. Hamed, A. M. Abdou, M. M. Kandil, E. M. Elbaz and D. S. Mikhail, *Drug Dev. Res.*, 2023, **84**, 475–499.
- 53 S. E. Seif, Z. Mahmoud, W. W. Wardakhan, A. M. Abdou and R. A. Hassan, *Drug Dev. Res.*, 2023, **84**, 839–860.
- 54 I. M. Salem, S. M. Mostafa, I. Salama, O. I. El-Sabbagh, W. A. H. Hegazy and T. S. Ibrahim, *J. Enzyme Inhib. Med. Chem.*, 2023, **38**, 203–215.
- 55 B. S. Ferreira, R. C. Silva, B. A. Souto and M. S. dos Santos, *Lett. Org. Chem.*, 2020, **18**, 335–343.
- 56 G. N. Tageldin, S. M. Fahmy, H. M. Ashour, M. A. Khalil, R. A. Nassra and I. M. Labouta, *Bioorg. Chem.*, 2018, **78**, 358–371.
- 57 P. Skehan, R. Storeng, D. Scudiero, A. Monks, J. McMahon, D. Vistica, J. T. Warren, H. Bokesch, S. Kenney and M. R. Boyd, *J. Natl. Cancer Inst.*, 1990, **82**, 1107–1112.
- 58 R. H. Shoemaker, *Nat. Rev. Cancer*, 2006, **6**, 813–823.
- 59 M. R. Boyd and K. D. Paull, *Drug Dev. Res.*, 1995, **34**, 91–109.
- 60 M. C. Alley, D. A. Scudiere, A. Monks, M. L. Hursey, M. J. Czerwinski, D. L. Fine, B. J. Abbott, J. G. Mayo, R. H. Shoemaker and M. R. Boyd, *Cancer Res.*, 1988, **48**, 589–601.
- 61 M. R. Grever, S. A. Schepartz and B. A. Chabner, *Semin. Oncol.*, 1992, **19**, 622–638.
- 62 T. Mosmann, *J. Immunol. Methods*, 1983, **65**, 55–63.
- 63 M. F. Tolba, A. Esmat, A. M. Al-Abd, S. S. Azab, A. E. Khalifa, H. A. Mosli, S. Z. Abdel-Rahman and A. B. Abdel-Naim, *IUBMB Life*, 2013, **65**, 716–729.
- 64 A. M. Rieger, K. L. Nelson, J. D. Konowalchuk and D. R. Barreda, *J. Visualized Exp.*, 2011, **50**, e2597.
- 65 M. McTigue, B. W. Murray, J. H. Chen, Y. L. Deng, J. Solowiej and R. S. Kania, *Proc. Natl. Acad. Sci. U. S. A.*, 2012, **109**, 18281–18289.
- 66 K. E. Anwer and G. H. Sayed, *J. Heterocycl. Chem.*, 2020, **57**, 2339–2353.
- 67 J. A. Pietenpol and Z. A. Stewart, *Toxicology*, 2002, **181–182**, 475–481.
- 68 W. Gorczyca, *Endocr.-Relat. Cancer*, 1999, **6**, 17–19.
- 69 I. Vermes, C. Haanen, H. Steffens-Nakken and C. Reutellingsperger, *J. Immunol. Methods*, 1995, **184**, 39–51.
- 70 C. L. J. Teng, C. T. R. Yu, W. L. Hwang, J. R. Tsai, H. C. Liu, G. Y. Hwang and S. L. Hsu, *Ann. Hematol.*, 2013, **92**, 301–313.
- 71 M. S. Taghour, H. A. Mahdy, M. H. Gomaa, A. Aglan, M. G. Eldeib, A. Elwan, M. A. Dahab, E. B. Elkaeed, A. A. Alsouk, M. M. Khalifa, I. H. Eissa and H. Elkady, *J. Enzyme Inhib. Med. Chem.*, 2022, **37**, 2063–2077.